Numerical modeling of aerosol deposition process

A. Zabihi Yeganeh, M. Jadidi, C. Moreau, A. Dolatabadi

PII: S0257-8972(19)30471-2
DOI: https://doi.org/10.1016/j.surfcoat.2019.04.094
Reference: SCT 24589

To appear in: *Surface & Coatings Technology*

Received date: 10 January 2019
Revised date: 29 April 2019
Accepted date: 30 April 2019

Please cite this article as: A.Z. Yeganeh, M. Jadidi, C. Moreau, et al., Numerical modeling of aerosol deposition process, Surface & Coatings Technology, https://doi.org/10.1016/j.surfcoat.2019.04.094

Numerical Modeling of Aerosol Deposition Process

A. Zabihi Yeganeh, M. Jadidi, C. Moreau and A. Dolatabadi*

Department of Mechanical, Industrial and Aerospace Engineering, Concordia University, Montreal, Quebec, H3G 1M8, Canada.

*Email: ali.dolatabadi@concordia.ca

Abstract

Aerosol Deposition (AD) method is an emerging coating process for deposition of ceramic particles for industrial applications such as MEMS, fuel cells, optical devices and radio frequency components. In this process, various parameters such as nozzle geometry, powder size and type, pressure inside the deposition chamber, and carrier gas flow rate have significant influence on the in-flight particle behavior before impact, and therefore, on the coating properties. In this study, a two-way coupled Eulerian-Lagrangian model is used to study the effects of gas flow rates and substrate location on the gas flow characteristics, bow shock near the substrate, and more importantly on the particle velocity and trajectory upon impact. The study is carried out with a rectangular sonic nozzle. To validate our simulations, locations of the Mach disks in highly under-expanded free-jet conditions are compared with the theoretical and experimental results in the literature. Two different computational geometries are utilized; a 2D planar and a quarter slice of 3D. It is found that, for the rectangular nozzle, the 3D geometry produces more accurate results and can capture the axis-switching phenomenon. Moreover, it is observed that the gas flow structure as well as the in-flight particle behavior obtained from 2D and 3D geometries are almost identical before the Mach disk. In addition, two different drag

expressions are employed and it is shown that the influence of Mach and Knudsen numbers on particle behavior in vacuum condition is significant.

Keywords: Aerosol deposition, Vacuum, Highly under-expanded jet, In-flight particle behavior, Drag force, Mach disk

List of symbols

C_D	Drag coefficient	
d_p	Particle diameter	m
k	Thermal conductivity	$\frac{\mathrm{W}}{\mathrm{m.K}}$
Kn	Knudsen number	
M	Mach number	
m_p	Particle mass	kg
Re	Reynolds number	
s	Molecular speed ratio	
St	Stokes number	
T	Temperature	K
u	Velocity	$\frac{\mathrm{m}}{\mathrm{s}}$
ρ	Density	$\frac{\mathrm{kg}}{\mathrm{m}^3}$
μ	Viscosity	$\frac{\mathrm{kg}}{\mathrm{m.s}}$

1. Introduction

Fabrication of ceramic coatings with thermal spray methods are associated with high operating temperatures close to the particle melting temperature, where particles are deposited on substrate in molten or semi-molten state. When particles are solidified on substrate, their phases are changed which can cause significant change on coating properties. For instance, alumina particles are in α phase when particles are in solid state. In case of rapid solidification, the alumina phase transfers from α to γ which is less wear resistance. It can be inferred that, the properties of final coating is dependent on the initial particles condition during the coating process. Also during the solidification process of molten particles, voids and cracks can be introduced between each layer of a lamellar structure. Finally, thermal spray processes are challenging for temperature sensitive substrates such as metals, glass and plastics. Therefore, the aerosol deposition method (also known as vacuum cold spray or vacuum kinetic spraying) was introduced to create highly dense ceramic coatings below particles melting point temperature in order to maintain the microstructure properties of both coating material and substrate [1-4].

The schematic of a typical aerosol deposition system is presented in figure 1. A compressed carrier gas such as nitrogen, air, argon or helium is mixed with micron-size ceramic particles inside the aerosol chamber to create the aerosol. Afterward, the aerosol is delivered through a nozzle in order to accelerate the particles to reach the adequate kinetic energy. The coating is built up by the impact of solid particles upon the substrate.

Aerosol deposition process usually occurs in vacuum condition with a deposition chamber pressure between 0.1 - 15 torr (10 - 2000 Pa). The pressure inside the aerosol chamber is typically between 45 - 800 torr (i.e. 6 - 106 kPa) and depends on nozzle geometry and carrier gas type and flow rate [4-6]. In general, when the aerosol is exhausted through the nozzle to the

deposition chamber, a highly underexpanded supersonic jet is created since the ambient pressure is much below the nozzle exit pressure. The physics of highly underexpanded supersonic jet can be found in the literature such as [7] and is described schematically in figure 2. In a few words, in the highly underexpanded regime, as the flow expands into the low-pressure ambient gas, an expansion fan forms at the nozzle lip. By interaction of these expansion waves with the free pressure jet boundary, weak compression waves are reflected. The compression waves merge to produce an intercepting shock in the interior of the jet. Behind the intercepting shock, the flow is still supersonic but at a lower Mach number compared to the flow in the jet's core. Furthermore, a slightly curved shock, which is normal to the flow at the jet axis and known as the Mach disk, is observed at a certain distance from the nozzle exit. Behind the Mach disk, the flow is theoretically subsonic. The location and strength of the Mach disk are not only dependent on the pressure ratio of nozzle inlet and deposition chamber but also depend on the diameter of the nozzle exit. The interaction of the Mach disk and intercepting shock forms another shock. The flow behind this reflected shock is still supersonic, where the second normal shock can happen similar to the first one as shown in figure 2. The location and diameter of first Mach disk is a function of pressure ratio and diameter of the nozzle's exit [7]. Prediction of Mach disk location is important for aerosol deposition simulation since it has a direct effect on particles velocity and trajectory. Shocks location can change the coating structure by affecting in-flight particles velocity.

Several studies have been done so far to increase the quality of ceramic coatings generated by aerosol deposition method and to find the optimum operating conditions. In 2001, Akedo and Lebedev [8] studied the influence of carrier gas on electrical and optical properties of $Pb(Zr,Ti)O_3$ coating. They showed that the carrier gas type (i.e. density) and velocity noticeably

affect the particle velocity which has significant influence on transmittance value of PZT thin films and their ferroelectric properties [8]. Despite the fact that coating properties depend strongly on the particles velocity, in another study [3], Akedo utilized helium and air as the carrier gases with flow rates ranging between 1-20 L/min and measured the velocity of micron sized alumina and PZT particles under various operating conditions. Velocity measurement was carried out using a time-of-flight method [9] in which a slit, which moved perpendicularly to the jet axis, was placed between the nozzle and substrate. In another work, a critical velocity around 150 m/s was estimated for adhesion of micron size particles upon impact [5]. The effect of particle velocity upon impact on coating structure was studied by Kwon et al. [10] who found that increasing the gas flow rate increases the velocity of the spray particles and facilitates the adhesive bonding. As a result, thicker coating can be achieved. In addition, the coating porosity was found to increase with higher gas flow rates.

Since non-intrusive methods for particles velocity measurement are difficult to apply due to the limited optical area inside the vacuum chamber and intrusive methods like time-of-flight method [9] changes the flow characteristics, numerical analysis of the gas and particles phases can be used to predict particle velocity, temperature, and trajectory. Numerical simulation is a powerful tool to understand the physics behind the aerosol deposition method and to propose optimum operating conditions to improve aerosol deposition process. One of the earliest numerical study was done by Katanoda and Matsuo [11] using a two-dimensional (2D) planar computational domain which was based on a slit nozzle with a rectangular cross section of 0.4×10 mm^2. Since the length of the cross section is much larger than its width, they assumed that the gas flow is 2D. Two different inlet pressures of 2 and 6 kPa were applied while the pressure inside the deposition chamber and stagnation temperature were set to 100 Pa and 300 K, respectively. It

was also assumed that the jet flow is laminar, therefore, no turbulence model was used. The effect of particles on gas flow were ignored as well. In their work, the drag coefficient proposed by Henderson [12], which considers the effects of Knudsen, Mach, and Reynolds numbers on the particle behavior, was employed. Moreover, a substrate was located at a standoff distance of 15 mm. In their study, the particle velocity predicted by the numerical simulation was compared with the experimental data, and a maximum error of 15% was reported. Park et al. [13] studied the effects of the geometry of circular nozzles and chamber pressure on the shock structure in aerosol deposition process using re-normalized group (RNG) $k-\varepsilon$ turbulence model and a 2D axisymmetric computational domain. The pressure inside the deposition chamber was varied between 1.316 and 100 kPa. It was shown that, to maximize the flow kinetic energy, the nozzle geometry should be adjusted to reach the fully expanded condition (i.e. the nozzle exit pressure is equal to ambient pressure). In other words, as the ambient pressure decreases, the nozzle exit diameter must be increased to reduce the shock formation and yield optimum condition. Similar results were reported experimentally and numerically by Lee et al. [14]. The in-flight behavior of Al_2O_3 particles accelerated with a helium jet in the aerosol deposition process was investigated by Park et al. [15]. In this study, the $k-\varepsilon$ realizable turbulence model was employed and the drag coefficient was dependent on Reynolds number solely (see the spherical drag coefficient in ANSYS [16]). It was shown that, generally, the particle velocity and the impact probability increase as the gas flow rate enhances. In addition, they revealed that the particle acceleration and deceleration, and the impact velocity, depend strongly on the particle size. Beside significant effect of gas flow rate, Chun et al. [17] reported in a numerical study that the standoff distance has a considerable impact on particle velocity. They used the shear stress transport RANS model with $k-\omega$ turbulence model in ANSYS-CFX [18] to predict the continuous gas phase

behaviour. For the particle phase, the Lagrangian tracking method was utilized and the drag force was considered to be the only effective force on particles during spraying. For the drag coefficient, the Schiller-Naumann drag correlation [19] was utilized in this study. Johnson et al. [20] also numerically studied the effects of particle size and standoff distance on particle velocity and trajectory upon impact using $k-\varepsilon$ realizable turbulence model and a 2D planar domain. The Schiller-Naumann drag correlation [19], which depends only on the Reynolds number, was used. It was shown that, although large particles have lower in-flight velocity compared to the small particles, they can easily pass the bow shock near the substrate without significant deceleration. They revealed that particles with diameters less than $0.5\,\mu m$, are easily decelerated and distracted near the substrate [20].

The main objectives of this study is to determine the influence of drag coefficient, three dimensional analysis and thermophoretic force on in-flight particles behaviour. In the current work, since sonic nozzles with circular cross sections have been widely used to investigate the highly underexpanded jets, at first, we model the gas flow through such a nozzle and compare the numerical results with the experimental data in the literature to validate our assumptions. Then, a slit nozzle with a rectangular cross section is assumed and 2D planar as well as 3D simulations of continuous phase are performed. It is worth mentioning that the cross section of the nozzle in aerosol deposition method is typically rectangular. By comparing the results of 2D planar and 3D simulations, we are able to explain when the assumption of 2D planar computational domain is applicable. In addition, some 3D phenomena such as axis-switching is illustrated. Subsequently, Al_2O_3 particles are injected and their in-flight behavior is simulated using two different drag coefficients. One of the drag coefficients is a function of the Reynolds number solely while the other one considers the effects of Reynolds, Mach and Knudsen

numbers. By comparing the results, the effects of gas compressibility and rarefaction on particle in-flight characteristics in aerosol deposition process can be observed and the appropriate drag coefficient can be found. After having an accurate model for both continuous and dispersed phases, the effect of gas flow rate and standoff distance are studied in order to predict the optimized operating condition for aerosol deposition system. The effect of thermophoretic force on the particle in-flight behavior is discussed in the last part.

2. Numerical method

In the current study, based on the pressure ratio range and the Knudsen number of the gas, the gas flow is assumed to be continuum and compressible [21] (similar assumptions can be found in other numerical studies such as [11, 13-15]). The Eulerian-Lagrangian approach with two-way coupling assumption as implemented in ANSYS-Fluent® release 14.5, is utilized [16]. It is worth mentioning that since the time-averaged (i.e. Reynolds-averaged) conservation equations as well as turbulence formulas were described in detail in our previous papers [22-24] and reference [16], only the main points and assumptions are reviewed here. For the gas phase, the compressible forms of mass, momentum and energy equations together with the ideal gas equation of state are solved. Noting that the viscous heating term is also included in our simulations. The kinetic theory is employed to calculate both gas viscosity and thermal conductivity. In addition, the realizable $k-\varepsilon$ model together with the standard wall function is used to simulate the turbulent flow.

The gas solver used in this study is pressure-based steady state and the gravitational effects are ignored. To discretize the conservation equations, the finite volume method with second-order upwind scheme is applied. The standard and the least squares cell based options are enabled for

pressure and gradient terms, respectively. Furthermore, for coupling of the velocity and pressure fields, the semi-implicit method for pressure-linked equations (SIMPLE) algorithm is used [16]. To obtain a converged solution for the gas phase, at least 100,000 iterations are done. Then, the ceramic particles are injected into the nozzle.

The particles are assumed to be solid, spherical and inert. To calculate the particle velocity and momentum, the particle motion equation which comprises the drag force is applied [25]. As mentioned in the introduction part, two different drag coefficients are utilized in the current work. The first one, given below, is the Schiller-Naumann drag expression [19]

$$C_D = \left(1 + 0.15{Re_p}^{0.687}\right)\left(\frac{24}{Re_p}\right) \quad \text{(Eq 1)}$$

$$Re_p = \frac{\rho_g |u_g - u_p| d_p}{\mu_g} \quad \text{(Eq 2)}$$

where ρ_g, u_g, μ_g, u_p, and d_p are gas density, velocity, viscosity, particle velocity, and particle diameter, respectively. The above correlation is widely used in high velocity conditions such as thermal sprays and employed recently by Johnson et al. [20] to predict the particle velocity in aerosol deposition process. The second drag coefficient used in this study was introduced by Loth [26] in 2008 and considers the effects of compressibility and rarefaction on the particle behavior. It should be pointed out here that, since the pressure inside the deposition chamber is very low, the particle Knudsen number increases significantly and may reach greater than unity. In addition, due to the existence of a highly underexpanded supersonic jet, the particle Mach number changes noticeably and might be much greater than 1. In other words, the Mach and Knudsen numbers may play a significant role and their influence on the particle in-flight behavior should be understood. Particles Mach number, Knudsen number and speed ratio are

defined as; $M_p = \frac{|\vec{u}-\vec{u}_p|}{\sqrt{\gamma RT}}$, $Kn_p = \sqrt{\frac{\pi\gamma}{2}}\left(\frac{M_p}{Re_p}\right)$ and $s = M_p\sqrt{\frac{\gamma}{2}}$ for dispersed phase. Subsequently, the Loth's drag coefficient is calculated as follows.

$$C_D = \frac{C_{D,Kn,Re}}{1+{M_p}^4} + \frac{{M_p}^4 C_{D,fm,Re}}{1+{M_p}^4} \qquad \text{for } \mathrm{Re_p} \le 45 \qquad \text{(Eq 3)}$$

$$C_D = \frac{24}{Re_p}\left[1 + 0.15{Re_p}^{0.687}\right]H_M + \frac{0.42\,C_M}{1+\frac{42500\,G_M}{{Re_p}^{1.16}}} \qquad \text{for } Re_p > 45 \qquad \text{(Eq 4)}$$

$$C_{D,fm,Re} = \frac{C_{D,fm}}{1+\left(\frac{C'_{D,fm}}{1.63}-1\right)\sqrt{\frac{Re_p}{45}}} \qquad \text{(Eq 5)}$$

$$C'_{D,fm} = \frac{(1+s^2)exp(-s^2)}{s^3\sqrt{\pi}} + \frac{(4s^4+4s^2-1)\,\mathrm{erf}(s)}{2s^4} \qquad \text{(Eq 6)}$$

$$C_{D,fm} = \frac{(1+s^2)exp(-s^2)}{s^3\sqrt{\pi}} + \frac{(4s^4+4s^2-1)\,\mathrm{erf}(s)}{2s^4} + \frac{2}{3s}\sqrt{\pi\frac{T_p}{T_\infty}} \qquad \text{(Eq 7)}$$

$$C_{D,Kn,Re} = C_{D,Re}f_{Kn} = \frac{24}{Re_p}\left(1 + 0.15{Re_p}^{0.687}\right)f_{Kn} \qquad \text{(Eq 8)}$$

$$f_{Kn} = \frac{1}{1+Kn_p\left[2.514+0.8\,\exp\left(\frac{-0.55}{Kn_p}\right)\right]} \qquad \text{(Eq 9)}$$

$$C_M = \frac{5}{3} + \frac{2}{3}tanh\left[3\ln(M_p+0.1)\right] \qquad \text{for } M_p \le 1.45 \qquad \text{(Eq 10)}$$

$$C_M = 2.044 + 0.2exp\left\{-1.8\left[\ln\left(\frac{M_p}{1.5}\right)\right]^2\right\} \qquad \text{for } M_p \ge 1.45 \qquad \text{(Eq 11)}$$

$$G_M = 1 - 1.525{M_p}^4 \qquad \text{for } M_p < 0.89 \qquad \text{(Eq 12)}$$

$$G_M = 0.0002 + 0.0008tanh\left[12.77(M_p - 2.02)\right] \quad \text{for } M_p > 0.89 \qquad \text{(Eq 13)}$$

$$H_M = 1 - \frac{0.258\,C_M}{1+514\,G_M} \qquad \text{(Eq 14)}$$

where γ, R, T and T_p are the ratio of specific heats, the gas constant, the gas temperature and the particles temperature, respectively.

In addition to the drag force, the thermophoretic force can affect the particle dynamics in the aerosol deposition process, especially near the substrate. This force is due to the temperature

gradient in the gas phase and is in the direction of decreasing temperature. In the last part of the paper, the thermophoretic force is added to the particle motion equation and its effects on the particle in-flight behavior is discussed. The thermophoretic force suggested by Talbot et al. [27] is used here

$$F_T = \frac{-6\pi {\mu_g}^2 d_p C_s}{\rho_g m_p} \frac{1}{1+6C_m Kn_p} \frac{k_g/k_p + 2C_t Kn_p}{1+2k_g/k_p+4C_t Kn_p} \frac{\nabla T}{T} \quad \text{(Eq 15)}$$

where m_p, k_g, and k_p are the particle mass, and the gas and the particle thermal conductivities, respectively. Moreover, C_s, C_m, and C_t are constants and equal to 1.17, 1.14, and 2.18, respectively. The above correlation is extensively used for a wide range of Knudsen numbers and thermal conductivity ratios.

The particle heat transfer is simulated by the lumped capacity method since the particle is homogenous and the Biot number is less than 0.1. The Nusselt number and the heat transfer coefficient are calculated using the Ranz-Marshal equation [28]. For more information about the particle motion and heat transfer equations, interested readers are referred to our previous paper [22].

3. Geometry, computation mesh, and boundary conditions

Firstly, a 2D axisymmetric computational domain is prepared to validate the continuous phase solver mentioned above. A circular converging nozzle with 13 mm length, and inlet and exit diameters of 10 and 2.25 mm, respectively, is utilized. The nozzle geometry is the same as that used in the experimental work of Crist et al. [7] to study of highly underexpanded sonic jets. Nitrogen with different flow rates (i.e. 3, 6 and 13 L/min) at 300 K is injected into the nozzle. Furthermore, based on the range of Knudsen number associated with the gas phase [21], no-slip boundary condition is imposed on the walls of the nozzle. The turbulent intensity at the inlet

boundary is assumed to be 10%. In figure 3, the computational grid as well as the boundary conditions are illustrated. In all the cases, the outlet pressure is fixed at 150 Pa.

After validation of the gas phase solver, a rectangular nozzle is utilized for the numerical simulation of both continuous and dispersed phases (since the spray nozzle in aerosol deposition process is usually a slit nozzle with a rectangular cross section). The geometry of this rectangular nozzle is the same as that used in the work of Naoe et al. [6]. As presented in figure 4, the inlet and exit areas of the nozzle are 8×10 and 0.4×10 mm^2, respectively. Assuming the symmetry of the process for the considered geometry, only one quarter of the nozzle and the external domain are taken into account. In figure 5, the computational domain and the boundary condition are revealed. Similar to our previous case, nitrogen at 300 K with a turbulent intensity of 10% is injected into the nozzle. The gas flow rates are set to 2.5, 5.0 and 7.5 L/min for the inlet boundary, while the outlet pressure is constant and equal to 150 Pa.

Afterwards, to study the effect of standoff distance, a flat rectangular substrate with a cross sectional area of 5×3 cm^2 and 2 mm thickness is placed perpendicular to the nozzle axis at different standoff distances (i.e. 4, 8 and 16 mm from the nozzle's exit). Figure 6 shows the computational domain as well as the boundary conditions for the impinging jet modeling. It is worth mentioning that, to analyze the effect of standoff distance, the nitrogen flow rate is fixed at 5.0 L/min and the outlet pressure is maintained at 150 Pa. In table 1, the parameters investigated using the 3D computational domain are summarized.

In addition to 3D simulations, the 2D planar assumption is applied to model the fluid flow through the rectangular nozzle shown in figure 4. As discussed in the introduction section, this assumption was employed by Katanoda and Matsuo [11] and Johnson et al. [20] to simulate the aerosol deposition process. The main goal here is to find when the assumption of 2D planar is

acceptable. In this analysis, the inlet boundary condition for the 3D and the 2D planar cases is assumed to be the constant mass flux. In other words, since the depth of the 2D planar model is infinitely long, the mass flow rate applied to the actual geometry is converted to the mass flux, to ensure that the inlet boundary condition is independent of the cross sectional area. The inlet boundary condition is the mass flux calculated from the 5 L/min of flow at standard condition crossing the inlet cross sectional area of $8 \times 10\ \mathrm{mm}^2$. So, the mass flux is constant and equal to $1.25\ \mathrm{kg/m^2 s}$ for both 2D planar and 3D cases. In this case, because the flow inside the nozzle is chocked, the stagnation pressure inside the nozzle is the same for different cross sectional areas (i.e. is independent of the cross sectional area) [29]. Similar trends are observed for other parameters like temperature, density and static pressure inside the nozzle. In this study, the outlet pressure is fixed at 150 Pa, and there is no substrate in the domain.

In computational fluid dynamics, mesh quality and cell size are crucial factors that affect the results' accuracy and CPU time. If the mesh quality is poor or its cell number is too low, the accuracy of the results is decreased. On the other hand, increasing the cell number causes the computational time to increase significantly. Therefore, in order to reach accurate results within reasonable computational time, mesh study should be performed. In this study, for the 3D free-jet case mentioned above, three hexahedral meshes with different cell sizes are generated; 1) coarse mesh with 800,000 cells, 2) fine mesh with 2,200,000 cells, and 3) ultra-fine mesh with 4,600,000 cells. Figure 7 shows the effects of cell size on the variations of velocity magnitude and Mach number along the jet centerline, where the gas inlet flow rate is 5.0 L/min. As can be observed, the results obtained from the mesh with 2,200,000 cells are almost identical to the results of mesh with 4,600,000 cells. Therefore, for the free jet analysis, the fine mesh with

2,200,000 cells is selected. Similar study is done when the substrate is present in the computational domain.

Spherical Al_2O_3 (alumina) particles, in solid state and at room temperature, are injected into the nozzle. The surface injection method together with the Rosin-Rammler diameter distribution method are applied [16]. In other words, the streams of particles with diameters defined by the Rosin-Rammler function are injected from each face on the inlet surface. The particle size distribution is obtained from the work of Naoe et al. [6], as revealed in figure 8. The particle mass flow rates are assumed to be 0.25, 0.5 and 0.75 g/min for carrier gas flow rates of 2.5, 5 and 7.5 L/min, respectively (similar linear trend is shown in the work of Johnson et al. [20]). Here with a rough estimation the ratio of powder to gas consumption is kept constant.

4. Results and discussion

In this study, by assuming a circular sonic jet, the gas phase solver is validated against experimental measurements of Mach disk location and Mach number upstream of the shock [7], for a wide range of operating conditions. Then, the results for continuous phase obtained from 3D and 2D planar computational domains are presented and compared with each other. Afterwards, the particle velocities resulting from two different drag expressions are compared with each other and with experimental data found in literature [6]. Subsequently, the impact of gas flow rate and standoff distance on particles in-flight characteristics and their distributions at the substrate are shown. At the end, the effect of the thermophoretic force on the particle velocity is discussed.

4.1. Validation

As stated in the introduction part, according to the nature of highly underexpanded jets, a strong normal shock, known as Mach disk, exists at a certain distance from the nozzle exit. The Mach disk location is heavily dependent on the nozzle pressure ratio. Indeed, by increasing the pressure ratio, the Mach disk moves farther downstream and the diameter of the Mach disk increases [7]. In our numerical simulations, nitrogen at 300 K with three different flow rates (i.e. 3, 6, and 13 L/min) is injected into a circular converging nozzle with an exit diameter of 2.25 mm, while the outlet pressure is fixed at 150 Pa. It is clear that each of these flow rates represents a unique pressure ratio between the inlet and the outlet boundaries. For instance, figure 9 shows the contour of Mach number for 13 L/min nitrogen flow rate at the inlet boundary. In table 2, the Mach disk location (X_m) as well as Mach number upstream of the Mach disk obtained from numerical simulations are compared with the experimental data given by Crist et al. [7]. As it can be seen, a good agreement is achieved, validating our assumptions and numerical model.

4.2. Effect of three dimensional analysis

After validating the gas solver, the 3D rectangular and the 2D planar simulations are run. Figures 10 and 11 demonstrate the comparison between the contours of velocity magnitudes and Mach numbers, resulting from these simulations. Moreover, the values of velocity magnitude and Mach number along the centerline of the nozzles are shown in figure 12. As can be observed, the Mach disk location and the flow structure behind the Mach disk are considerably different. In the 3D simulation, the Mach disk is captured and the flow reaches the subsonic condition shortly. However, in 2D planar case, the flow expansion is much longer and the occurrence of Mach disk is not clear. In addition, the flow behind the strong shock is supersonic for a long distance (where the velocity is around 400 m/s) and a structure like shock diamonds can be observed. It is worth

mentioning that, near the nozzle exit (i.e. before the Mach disk location in the 3D case (standoff distance less than around 10 mm)), both 3D and 2D planar simulations predict similar results. It should be noted that, knowing the Mach number distribution is useful since it provides important information regarding the flow regimes and has significant influence on the particles drag coefficient, and therefore, the in-flight particles behavior.

Jet-axis switching is probably the main reason why the results of 2D planar and 3D simulations are not consistent. It is established in the literature that, for non-circular three-dimensional jets, a major change in the jet's cross-sectional shape occurs with increasing the downstream distance from the orifice [30]. Although the jet cross section is highly skewed at first, it evolves through near circularity and then becomes skewed in the direction perpendicular to that of the initial skewness [30]. This phenomenon, obtained from our simulations, can be seen in figure 13. In this figure, the velocity magnitude iso-surfaces and their contours at various standoff distances (SD) are displayed. It clearly shows that, by increasing the downstream distance from the nozzle exit, the rectangular jet originated from a horizontal slot stretches vertically. It is obvious that the axis-switching phenomenon as well as Mach disk formation are not captured by the 2D planar simulations and can affect the calculated particle in-flight behavior. Hereafter, the 3D computational domain is employed to study the effects of gas flow rate and substrate presence on the flow structure, and to analyze the particle in-flight characteristics.

4.3. Effect of gas flow rate on continuous phase

Figures 14 and 15 show the dependency of the velocity magnitude, Mach number and Mach disk location and diameter on the gas flow rate. In general, increasing the gas flow rate (from 2.5 to 5 and 7.5 L/min) causes the velocity magnitude, Mach number and Mach disk location and

diameter as well as the jet angle to increase. This outcome is consistent with the experimental results in the literature [7].

4.4. Effect of standoff distance on continuous phase

Figures 16 and 17 illustrate the influence of substrate presence and standoff distance on the gas flow structure, velocity magnitude, Mach number, and bow shock formation and strength. As mentioned in the introduction part, a flat rectangular substrate is located at 4, 8 and 16 mm from the nozzle exit. Again, the outlet pressure and the gas flow rate are fixed at 150 Pa and 5 L/min, respectively. It is clearly shown in these figures that, as the gas approaches the substrate, its axial velocity as well as the Mach number significantly decrease while the static pressure on the substrate dramatically increases. This region is called stagnation or deceleration region and can significantly affect the particle impact velocity and angle. It can also cause the particles with low Stokes number to decelerate and follow the gas streamlines without impacting the substrate (for more information regarding the effects of Stokes number, see [24, 31]). Figure 18 shows the stagnation or the high pressure region near the substrate at various standoff distances. As can be observed from figures 16-18, the bow shock formation and strength as well as the pressure distribution on the substrate depend on the substrate location and Mach disk. When the standoff distance is less than the Mach disk distance, a bow shock is formed near the substrate (see the cases with standoff distances of 4 and 8 mm). In this condition, increasing the standoff distance causes the strength of bow shock and the pressure value on the substrate to reduce. However, the surface area of the stagnation region increases with the standoff distance. If the standoff distance is slightly more than the Mach disk distance, the flow structure becomes more complex due to the interaction of the Mach disk and a possible bow shock. For example, in our simulations when

the standoff distance is 16 mm, the Mach disk is formed at first. Behind the Mach disk, there is a high pressure region with low velocity and Mach number (see figures 16c, 17c, and 18c). Afterwards, the velocity and Mach number increase and the gas approaches the substrate. Here, since the flow is supersonic near the substrate, a bow shock is formed and the pressure on the substrate increases. This is the reason why, in figure 18c, two high pressure regions are presented. It is also worth mentioning that, for the standoff distance of 16 mm, the high pressure region on the substrate is vertical due to the axis-switching phenomenon. As a final point, when the substrate location is far behind the Mach disk, where the gas flow is subsonic, the bow shock near the substrate cannot be theoretically formed.

4.5. Effect of drag force expression and three dimensional analysis on particles phase

In the current work, the in-flight particle behaviour is analyzed using two different drag expressions (i.e. Loth [26] and Schiller-Naumann [19]) and two computational geometries (i.e. 2D planar and 3D). In figure 19, the effects of drag coefficient and gas compressibility and rarefaction on the particle velocity are revealed. Similar to other numerical studies in this field (e.g. see [11, 20, 32]) the 2D planar simulation is run, and the velocities of the particles located at the standoff distance of 8 mm are captured. As can be observed, compared to the Schiller-Naumann drag expression, the Loth's drag expression that considers the effects of compressibility and rarefaction predicts much lower particles velocities with a narrower distribution. In table 3, the comparison between numerical results and experimental data obtained from particle image velocimetry (PIV) [6] is presented. The calculated errors and standard deviations verify that the Loth's drag expression [26] predicts more accurate results, and is utilized in this study hereafter. In other words, in aerosol deposition process, since the particle

diameter is very small and the vacuum condition exists, the Mach and Knudsen numbers play significant roles and their effects must be taken into account.

Figures 20 shows the particle velocity distributions at the standoff distances of 8 mm, obtained from 2D planar and 3D simulations with the constant mass flux inlet boundary condition mentioned above. As presented, using the 3D simulation, the particle velocity distribution is around 195 m/s which is close to the value for 2D planar model. By increasing the standoff distance to 16 mm, the results of particle velocity distribution obtained from 2D planar and 3D simulations are more different (see figure 21). It is shown that by using 3D simulation, particles velocity distribution becomes slightly narrower and shifts to the left. This is due to difference between predicted gas velocities particularly after the Mach disk (see figures 10-12).

4.6. Effect of gas flow rate on particle phase

As discussed above and shown in figures 14 and 15, the gas flow rate has significant influence on the pressure of aerosol chamber, and the jet velocity profile and Mach number. Therefore, it is reasonable to expect that the particle in-flight behavior changes with the gas flow rate. Figure 22 demonstrates the particles velocity distributions for different gas flow rates at the standoff distance of 8 mm. As can be seen, in general, increasing the gas flow rate causes the velocity distribution to be wider and the average velocity to enhance. The average particle velocity for 2.5, 5, and 7.5 L/min gas flow rates are 163, 195, and 221 m/s, respectively.

4.7. Effect of standoff distance on particle phase

In the aerosol deposition process, the particles normal velocity upon impact is important and controls the coating quality. To study the effects of standoff distance, Mach disk, and bow shock on the particle trajectory and velocity, the substrate is located at 4, 8 and 16 mm from the exit of

the nozzle while the gas flow rate is fixed at 5 L/min. Figures 23 reveals the particle velocity and trajectory during flight and near the substrate for different standoff distances. As one can see, in general, smaller particles have higher velocities. In addition, it seems that the particle velocity is not a strong function of the standoff distance. However, for standoff distance of 16 mm, the trajectories of a few particles (i.e. those that are away from the jet centerline) are affected near the substrate, mainly due to the existence of jet axis-switching.

In order to determine the dependency of particle normal velocity on the substrate location, the velocity distributions at various standoff distances, while the gas flow rate is fixed at 5 L/min, are shown in Figure 24. This figure verifies that the particle normal velocity is almost independent of substrate location and standoff distance, because the Stokes number of the particles is on the order of magnitude of 1000. Similar to other papers [33, 34], the Stokes number is defined as the ratio of particle response time to the characteristic time of the flow. It is related to the ratio of the particle's inertia and the drag force ($St = 4m_p u_p / 6\pi\mu_g {d_p}^2 = \rho_p d_p u_p / 9\mu_g$, where ρ_p is the particle density). Obviously, a particle with a low Stokes number follows the gas streamlines while a particle with a high Stokes number is less affected by the gas flow and tracks its own trajectory. In this figure, the particle velocity profile for a free jet (without substrate) at 8 mm from the nozzle exit is also illustrated. It clarifies that the substrate presence causes the particle velocity to reduce slightly, owing to occurrence of the bow shock and the stagnation region.

The landing condition of the particles on the substrates with the standoff distances of 4, 8, and 16 mm is shown in Figure 25. The gas flow rate and the outlet pressure are kept constant and equal to 5 L/min and 150 Pa, respectively. The information provided here can be useful to understand where the particles land and how the coating is built-up. As presented, generally, the particles

land along the major axis of the jet. However, by increasing the standoff distance, the particles with low Stokes number (e.g. small particles as well as large particles with low velocity magnitude) are deflected from the major axis towards the minor axis of the rectangular jet due to the axis-switching phenomenon. In a word, Figures 23-25 show that particles with diameters of 1-6 μm have sufficient kinetic energy to overcome the Mach disk, the bow shock, and the stagnation region, and reach the substrate without significant deceleration and deflection.

4.8. Effect of thermophoretic force on particle velocity

As mentioned in the introduction part, the thermophoretic force is in a direction opposite to the gas temperature gradient (i.e. it is directed towards lower gas temperature [35]) and can affect the behavior of small particles. Figure 26 shows the effect of thermophoretic force on the particle normal velocity upon impact. Here, the substrate distance from the nozzle exit is 8 mm, the nitrogen flow rate is 5.0 L/min, and the outlet pressure is 150 Pa. Adding the thermophoretic force results in a slight reduction of particle impact velocity, due to the presence of stagnation or high temperature region near the substrate as illustrated in Figure 27.

5. Conclusion

In the current study, a two-way coupled Eulerian-Lagrangian model was used to simulate the aerosol deposition process and to understand the effects of gas flow rates and substrate location on the particle in-flight characteristics. It was shown that, for a rectangular sonic nozzle, a 3D simulation is needed to capture the Mach disk as well as the axis-switching phenomenon. In addition, it was found that increasing the gas flow rate causes the gas velocity magnitude, Mach disk location and diameter, and the particle velocity to increase. It was also shown that the bow

shock formation and strength as well as the pressure distribution on the substrate depend on the locations of substrate and Mach disk. Moreover, it was found that the particle velocity does not significantly vary with the standoff distance. Furthermore, it was revealed that the compressibility and rarefaction effects on the drag of particles are not negligible and must be taken into account for accurate computation results. In addition, the thermophoretic force results in a slight decrease of particle impact velocity.

Acknowledgment

The authors gratefully acknowledge the financial support from Natural Sciences and Engineering Research Council (NSERC) of Canada. This research was undertaken, in part, thanks to funding from the Canada Research Chairs Program.

References

[1] P.L. Fauchais, J.V.R. Heberlein, M. Boulos, Thermal Spray Fundamentals from Powder to Part, Springer, New York, 2014.

[2] J. Akedo, Aerosol deposition of ceramic thick films at room temperature: Densification mechanism of ceramic layers, J. Am. Ceram. Soc. 89 (2006) 1834–1839.

[3] J. Akedo, Room temperature impact consolidation (RTIC) of fine ceramic powder by aerosol deposition method and applications to microdevices, J. Therm. Spray Technol. 17 (2008) 181–198.

[4] D. Hanft, J. Exner, M. Schubert, T. Stocker, P. Fuierer, R. Moos, An overview of the aerosol deposition method: process fundamentals and new trends in materials applications, J. Ceram. Sci. Technol. 6 (2015) 147–182.

[5] J. Akedo, Aerosol deposition method for room-temperature ceramic coating and its applications, in: Shigeyuki Somiya, (Ed.) Handbook of Advanced Ceramics: Materials, Applications, Processing, and Properties, 2nd ed., Elsevier, 2013, pp. 847–860.

[6] K. Naoe, M. Nishiki, A. Yumoto, Relationship between impact velocity of Al2O3 particles and deposition efficiency in aerosol deposition method, J. Therm. Spray Technol. 22 (2013) 1267–1274.

[7] S. Crist, D.R. Glass, P.M. Sherman, Study of the highly underexpanded sonic jet, AIAA J. 4 (1966) 68–71.

[8] J. Akedo, M. Lebedev, Influence of carrier gas conditions on electrical and optical properties of Pb(Zr,Ti)O3 thin films prepared by aerosol deposition method, Jpn. J. Appl. Phys. 40 (2001) 5528–5532.

[9] M. Lebedev, J. Akedo, K. Mori, T. Eiju, Simple self-selective method of velocity measurement for particles in impact-based deposition, J. Vac. Sci. Technol. A 18 (2000) 563–566.

[10] J. Kwon, H. Park, I. Lee, C. Lee, Effect of gas flow rate on deposition behavior of Fe-based amorphous alloys in vacuum kinetic spray process, Surf. Coatings Technol. 259 (2014) 585–593.

[11] H. Katanoda, K. Matsuo, Gasdynamic simulation of aerosol deposition method, Mater. Trans. 47 (2006) 1620–1625.

[12] C.B. Henderson, Drag coefficients of spheres in continuum and rarefied flows, AIAA J. 14 (1976) 707–708.

[13] J.J. Park, M.W. Lee, S.S. Yoon, H.Y. Kim, S.C. James, S.D. Heister, S. Chandra, W.H. Yoon, D.S. Park, J. Ryu, Supersonic nozzle flow simulations for particle coating applications: Effects of shockwaves, nozzle geometry, ambient pressure, and substrate

location upon flow characteristics, J. Therm. Spray Technol. 20 (2011) 514–522.

[14] M.W. Lee, J.J. Park, D.Y. Kim, S.S. Yoon, H.Y. Kim, D.H. Kim, S.C. James, S. Chandra, T. Coyle, J. Ryu, W.H. Yoon, D.S. Park, Optimization of supersonic nozzle flow for titanium dioxide thin-film coating by aerosol deposition, J. Aerosol Sci. 42 (2011) 771–780.

[15] H. Park, H. Kwon, C. Lee, Inflight particle behavior in the vacuum kinetic spray process, J. Therm. Spray Technol. 26 (2017) 1616–1631.

[16] ANSYS Inc., ANSYS FLUENT Theory Guide, USA, 2012.

[17] D.M. Chun, J.O. Choi, C.S. Lee, S.H. Ahn, Effect of stand-off distance for cold gas spraying of fine ceramic particles (<5μm) under low vacuum and room temperature using nano-particle deposition system (NPDS), Surf. Coatings Technol. 206 (2012) 2125–2132.

[18] ANSYS Inc., ANSYS CFX-Solver Theory Guide, USA, 2006.

[19] L. Schiller, Z. Naumann, A drag coefficient correlation, Z. Ver. Deutsch. Ing. 77 (1935) 318–320.

[20] S.D. Johnson, D. Schwer, D.S. Park, Y.S. Park, E.P. Gorzkowski, Deposition efficiency of barium hexaferrite by aerosol deposition, Surf. Coatings Technol. 332 (2017) 542–549.

[21] J. F. O'Hanlon, A User's Guide to Vacuum Technology, 3rd ed., Wiley, New York, 2003.

[22] M. Jadidi, S. Moghtadernejad, A. Dolatabadi, A comprehensive review on fluid dynamics and transport of suspension/liquid droplets and particles in high-velocity oxygen-fuel (HVOF) thermal spray, Coatings 5 (2015) 576–645. https://doi.org/10.3390/coatings5040576.

[23] M. Jadidi, S. Moghtadernejad, A. Dolatabadi, Numerical modeling of suspension HVOF spray, J. Therm. Spray Technol. 25 (2016) 451–464.

[24] M. Jadidi, A.Z. Yeganeh, A. Dolatabadi, Numerical study of suspension HVOF spray and particle behavior near flat and cylindrical substrates, J. Therm. Spray Technol. 27 (2018) 59-72.

[25] C. Crowe, J.D. Schwarzkopf, M. Sommerfeld, Y. Tsuji, Multiphase Flow with Droplets and Particles, 2nd ed., CRC Press, Boca Raton, FL, 2011.

[26] E. Loth, Compressibility and rarefaction effects on drag of a spherical particle, AIAA J. 46 (2008) 2219–2228.

[27] L. Talbot, R.K. Cheng, R.W. Schefer, D.R. Willis, Thermophoresis of particles in a heated boundary layer, J. Fluid Mech. 101 (1980) 737–758.

[28] Y.A. Cengel, Heat and Mass Transfer: A Practical Approach, 3rd ed., McGraw-Hill, New York, 2006.

[29] Y.A. Cengel, M.A. Boles, Thermodynamics: an Engineering Approach, eighth ed., McGraw-Hill, New York, 2015.

[30] J.M. Gorman, E.M. Sparrow, J.P. Abraham, Slot jet impingement heat transfer in the presence of jet-axis switching, Int. J. Heat Mass Transf. 78 (2014) 50–57.

[31] M. Jadidi, M. Mousavi, S. Moghtadernejad, A. Dolatabadi, A three-dimensional analysis of the suspension plasma spray impinging on a flat substrate, J. Therm. Spray Technol. 24 (2015) 11–23.

[32] H. Katanoda, M. Fukuhara, N. Iino, Numerical simulation on impact velocity of ceramic particles propelled by supersonic nitrogen gas flow in vacuum chamber, Mater. Trans. 48 (2007) 1463–1468.

[33] G.G. Joseph, R. Zenit, M.L. Hunt, A.M. Rosenwinkel, Particle-wall collisions in a viscous fluid, J. Fluid Mech. 433 (2001) 329–346.

[34] P. Gondret, M. Lance, L. Petit, Bouncing motion of spherical particles in fluids, Phys. Fluids 14 (2002) 643.

[35] M.A. Gallis, D.J. Rader, J.R. Torczynski, A generalized approximation for the thermophoretic force on a free-molecular particle, Aerosol Sci. Technol. 38 (2004) 692–706.

Tables

Table 1 Investigated process parameters

Investigated Parameters	Flow rate (L/min)	Standoff distance (mm)	Powders flow rate (g/min)
Flow rate effect	2.5, 5.0, 7.5	Free jet	0.25, 0.5, 0.75
Standoff distance effect	5.0	4, 8, 16	0.5

Table 2 Mach disk location and Mach number upstream of the shock obtained from experiment [7] and numerical simulation

Flow rate	**3 L/min**	**6 L/min**	**13 L/min**
$X_m(Exp)$	10.3 mm	15.8 mm	20.9 mm
$X_m(Num)$	10.4 mm	16.1 mm	21.4 mm
$M_{max}(Exp)$	6.2	7.5	8.4
$M_{max}(Num)$	6	7.2	8.2

Table 3 Particle velocity data at 8 mm distance from the nozzle exit; Numerical results (using Loth [26] and Schiller-Naumann [19] drag expressions and 2D planar approach) vs PIV experimental data [6]

Velocity / Drag	Maximum	Minimum	Average	Standard deviation	Error (%)
Loth	342 m/s	67 m/s	190 m/s	87	5
Schiller-Naumann	725 m/s	77 m/s	263 m/s	206	30
Particles average velocity measured with PIV method by Naoe et al. [6] = 200.3 m/s					

List of figure captions

Figure 1 Schematic of aerosol deposition system

Figure 2 Schematic of a highly underexpanded jet

Figure 3 2D axisymmetric computational domain for circular sonic nozzle

Figure 4 Geometry of the rectangular nozzle

Figure 5 Computational domain for free-jet modeling (one quarter of the rectangular nozzle)

Figure 6 Computational domain for impinging jet modeling (one quarter of the rectangular nozzle)

Figure 7 (a) Velocity magnitude and (b) Mach number along the free-jet centerline for different grid sizes

Figure 8 Particle size distribution

Figure 9 Contour of Mach number for a circular converging nozzle with 13 L/min nitrogen flow rate

Figure 10 Contour of velocity magnitude for a rectangular nozzle, obtained from 2D planar and one quarter 3D assumptions

Figure 11 Contour of Mach number for a rectangular nozzle, obtained from 2D planar and one quarter 3D assumptions

Figure 12 (a) Velocity magnitude and (b) Mach number along the nozzle centerline for the 2D planar and one quarter 3D simulations

Figure 13 Velocity magnitude iso-surface (top) and contours at different standoff distance (bottom) with 5 L/min gas flow rate; SD stands for standoff distance

Figure 14 Contour of velocity magnitude for nitrogen flow rates of a) 2.5, b) 5 and c) 7.5 L/min

Figure 15 Contour of Mach number for nitrogen flow rates of a) 2.5, b) 5 and c) 7.5 L/min

Graphical Abstract

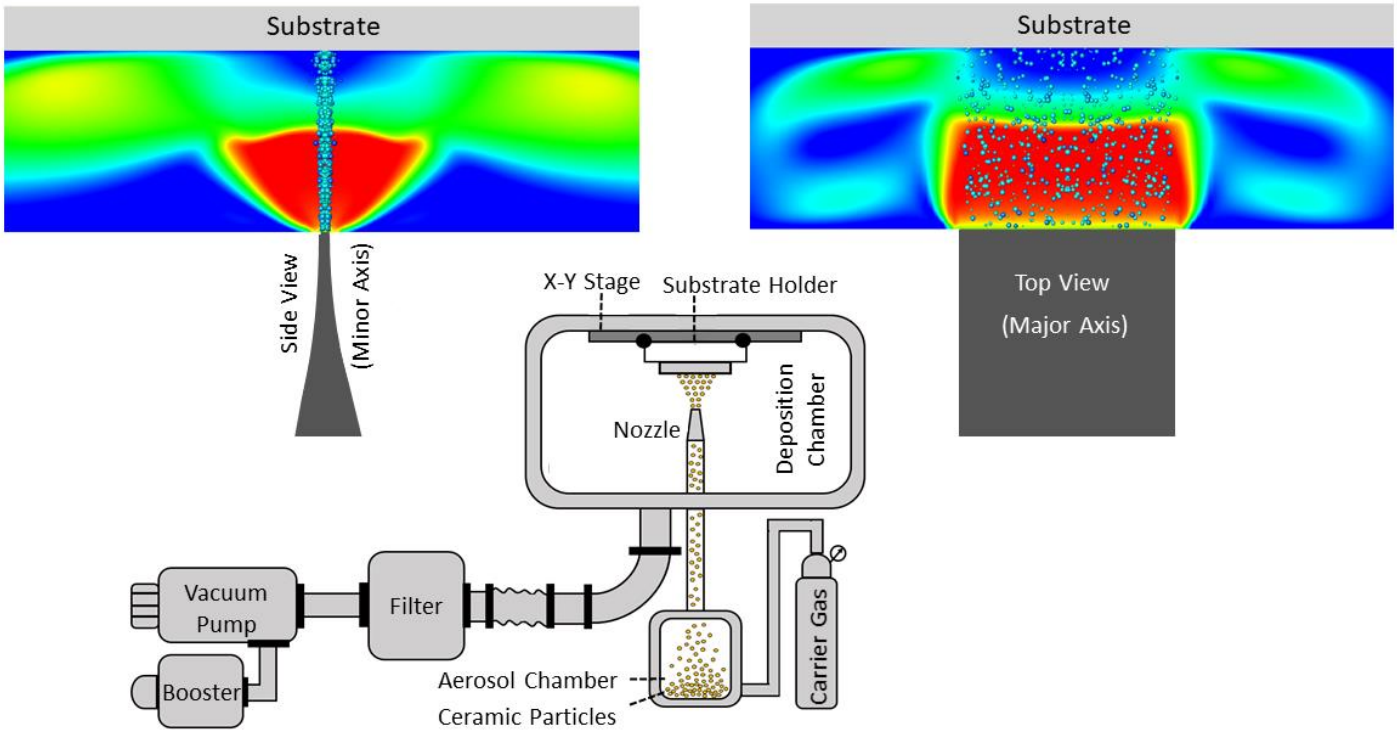

Highlights

- A precise numerical simulation is provided to predict the in-flight particles condition during the aerosol deposition.
- The result of free jet for 2D and 3D are compared with each other to show the effect of 3D analysis on gas flow behavior.
- Two different drag forces are compared to show the importance of Mach number and Knudsen number on coating particles characteristics upon impact. Due the large temperature gradient during the spray, the effect of thermophoretic force is also studied in this work.
- The effects of gas flow rate and standoff distance are studied for both gas and particles phase.

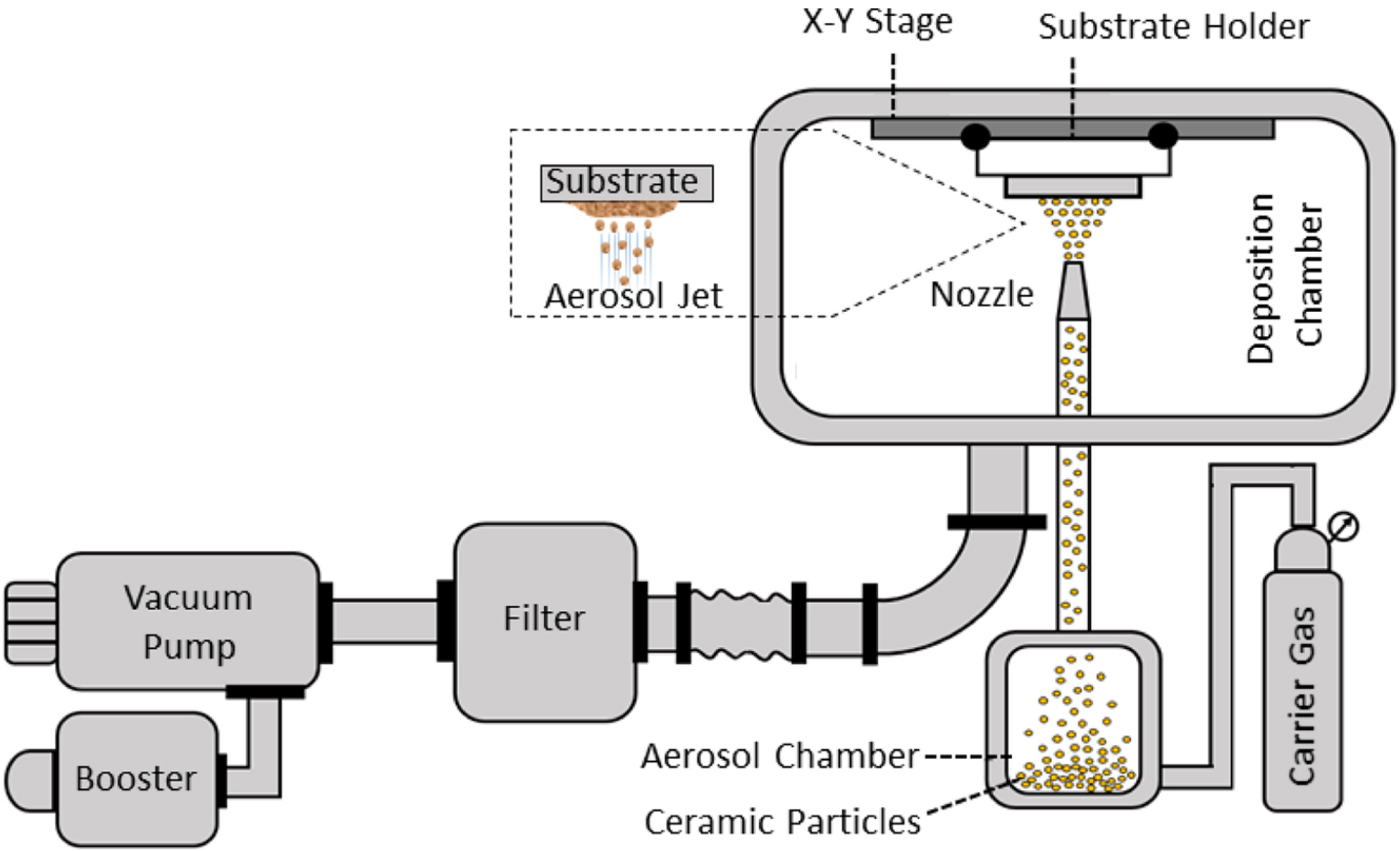
X-Y Stage
Substrate Holder
Substrate
Aerosol Jet
Nozzle
Deposition Chamber
Vacuum Pump
Filter
Booster
Aerosol Chamber
Ceramic Particles
Carrier Gas

Figure 1

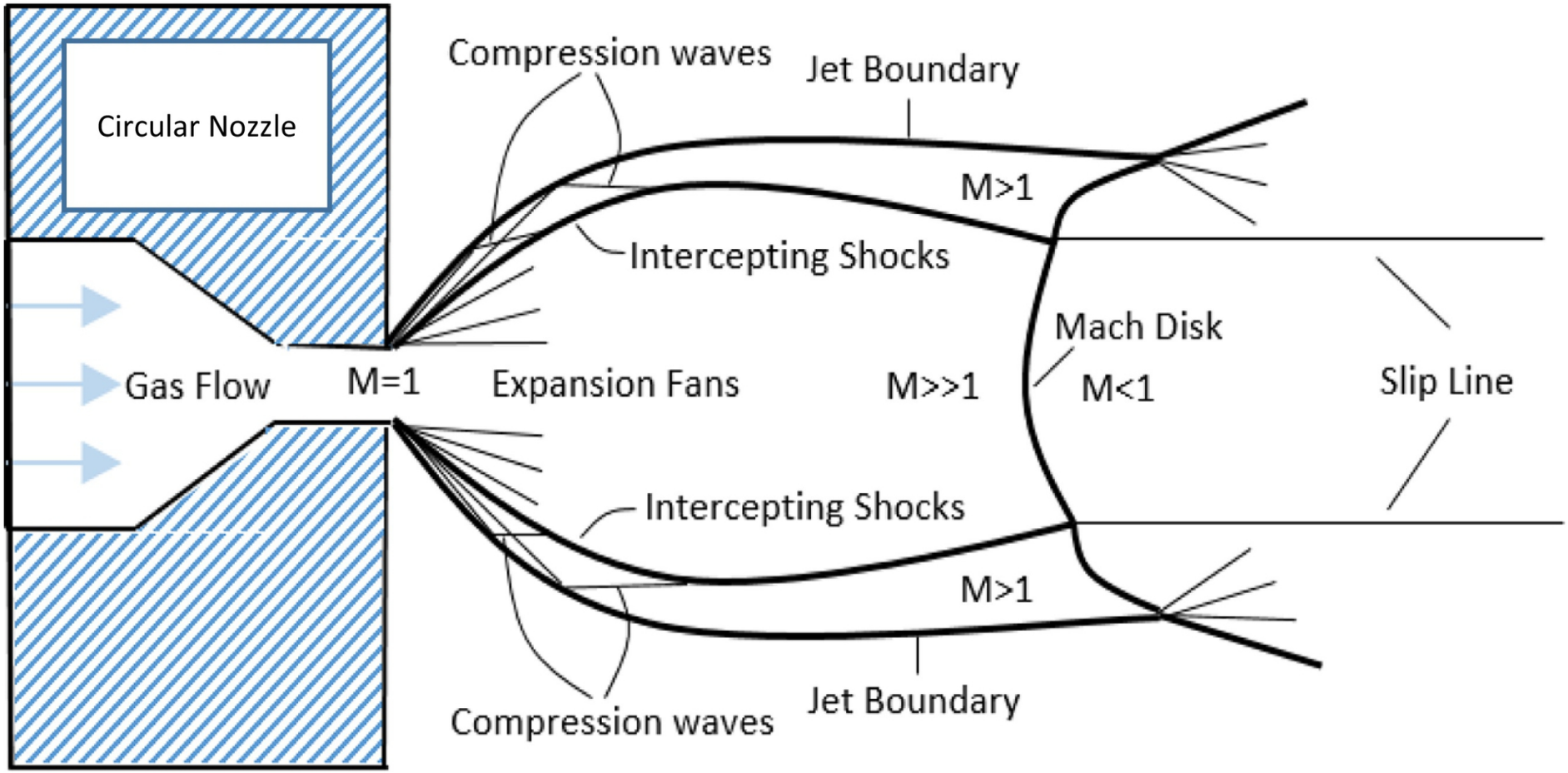
Circular Nozzle
Compression waves
Jet Boundary
M>1
Intercepting Shocks
Mach Disk
Gas Flow
M=1
Expansion Fans
M>>1
M<1
Slip Line
Intercepting Shocks
M>1
Jet Boundary
Compression waves

Figure 2

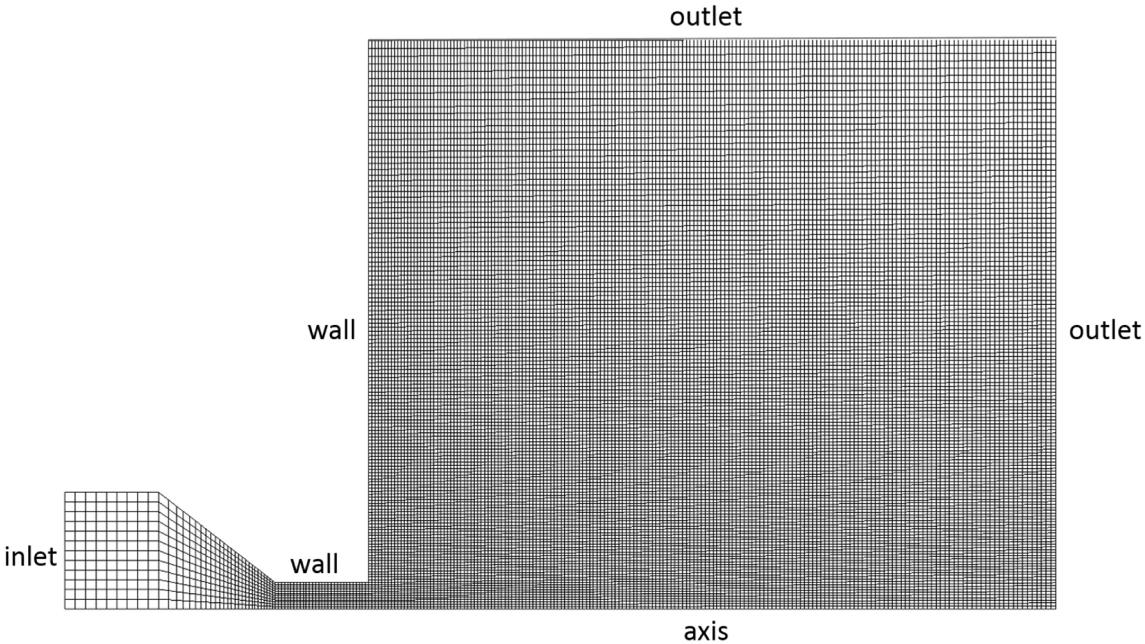

Figure 3

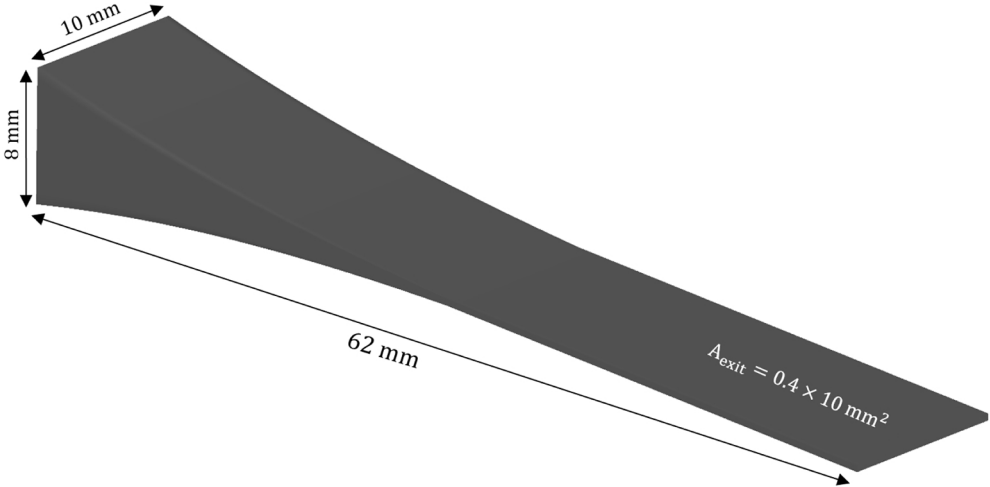

Figure 4

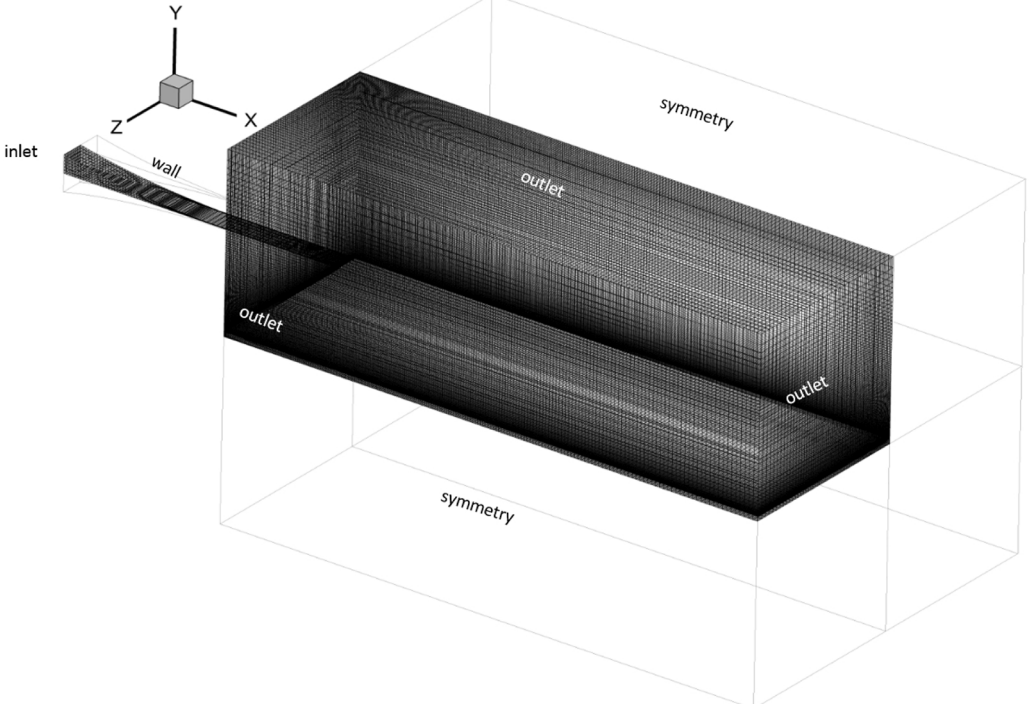

Figure 5

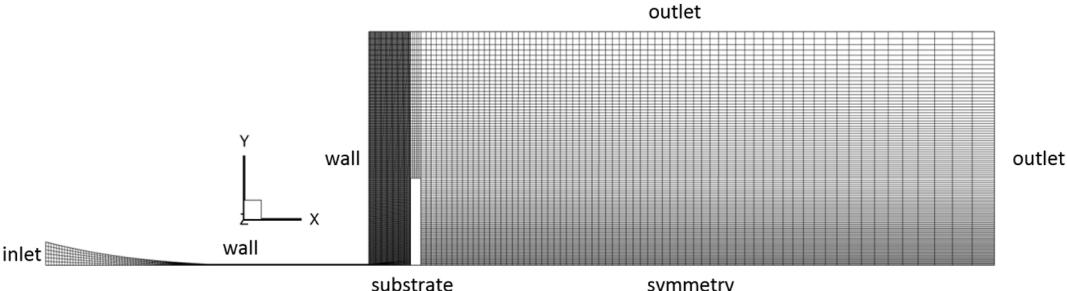

Figure 6

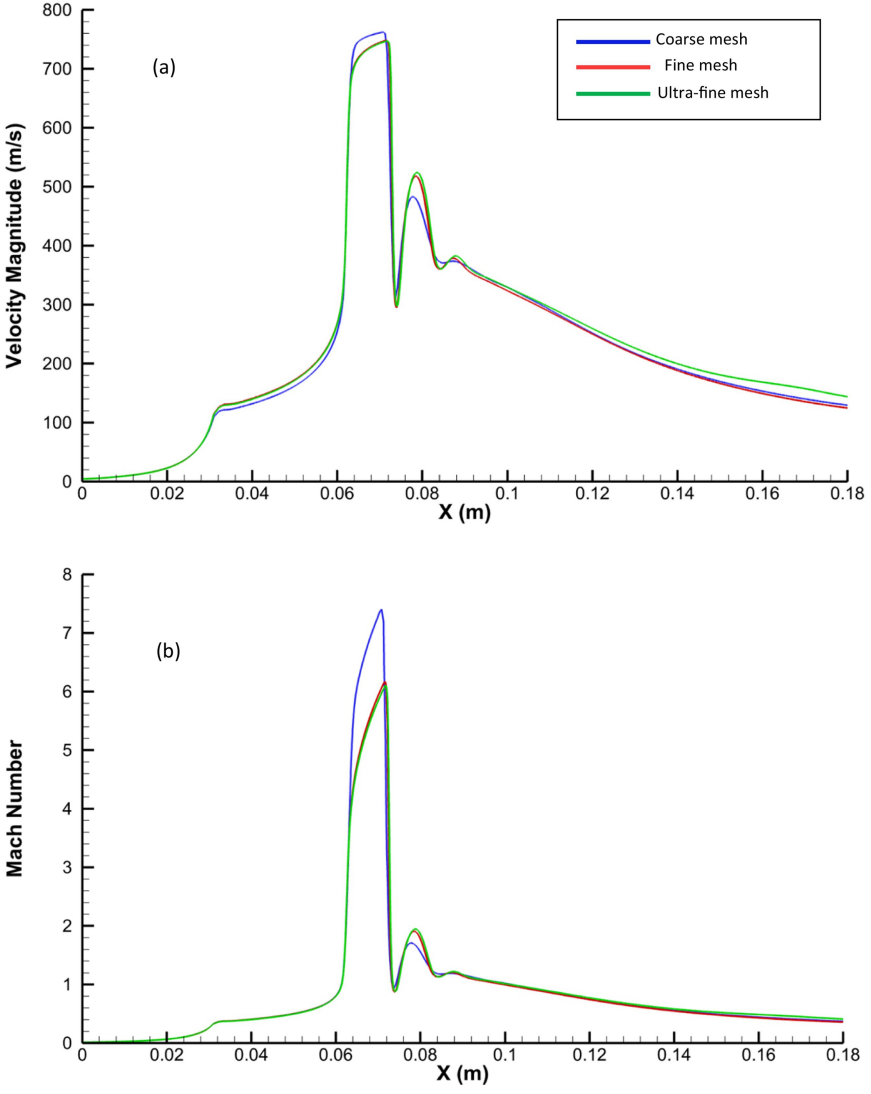
(a)
Coarse mesh
Fine mesh
Ultra-fine mesh
Velocity Magnitude (m/s)
X (m)
(b)
Mach Number
X (m)

Figure 7

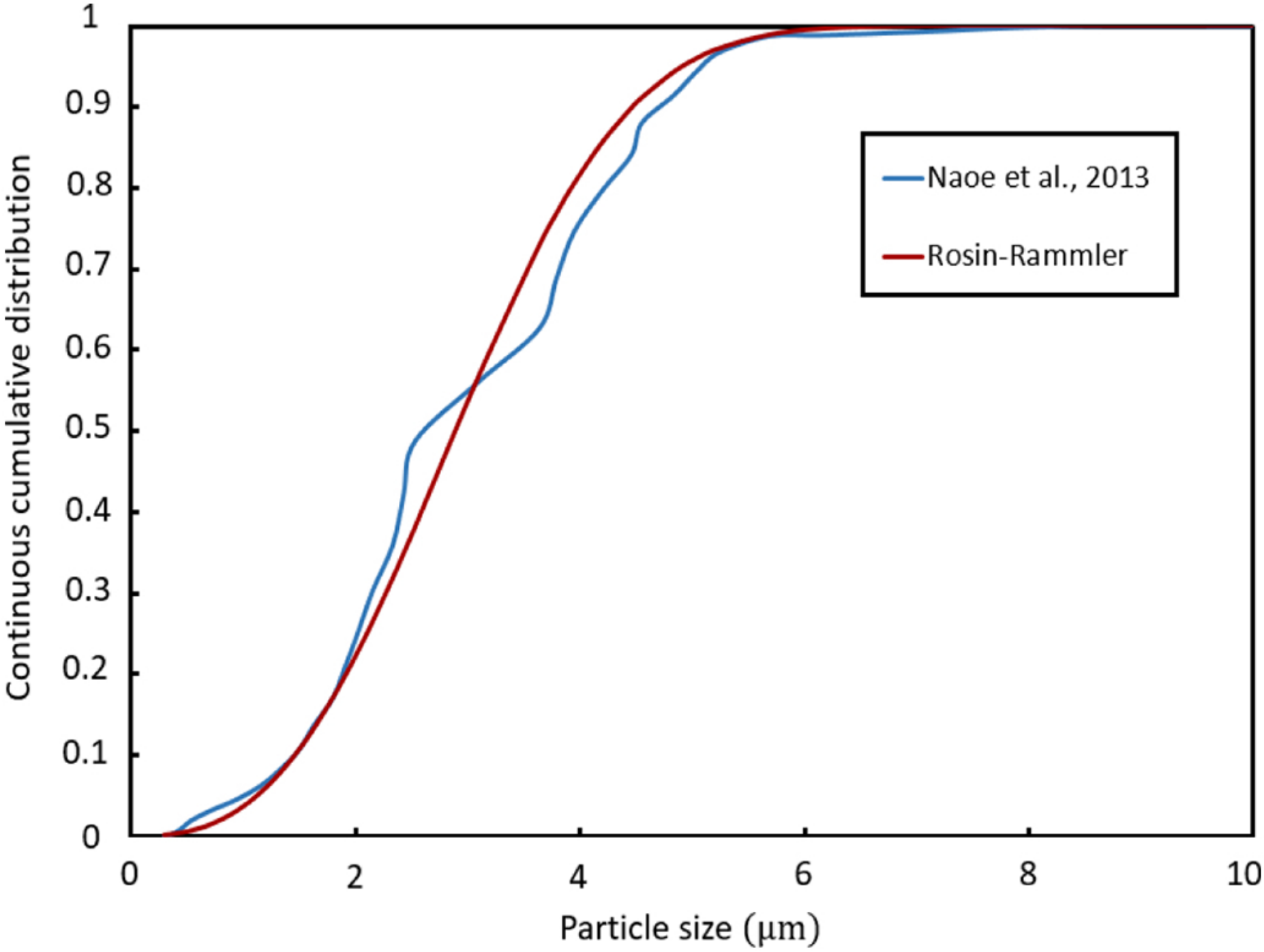
Continuous cumulative distribution
1
0.9
0.8
0.7
0.6
0.5
0.4
0.3
0.2
0.1
0
0
2
4
6
8
10
Particle size (μm)
Naoe et al., 2013
Rosin-Rammler

Figure 8

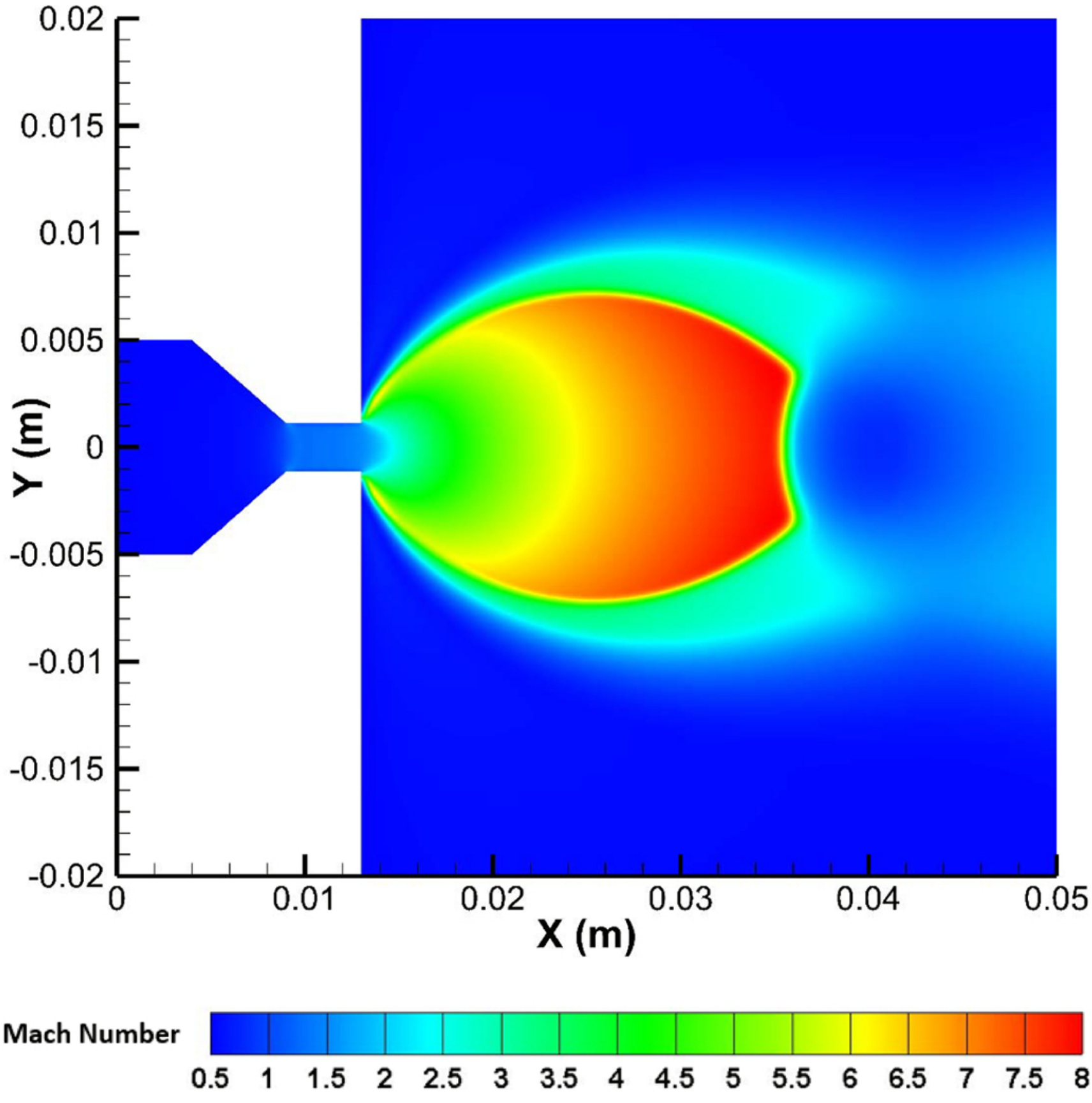
0.02
0.015
0.01
0.005
0
-0.005
-0.01
-0.015
-0.02
Y (m)
0
0.01
0.02
0.03
0.04
0.05
X (m)
Mach Number
0.5
1
1.5
2
2.5
3
3.5
4
4.5
5
5.5
6
6.5
7
7.5
8

Figure 9

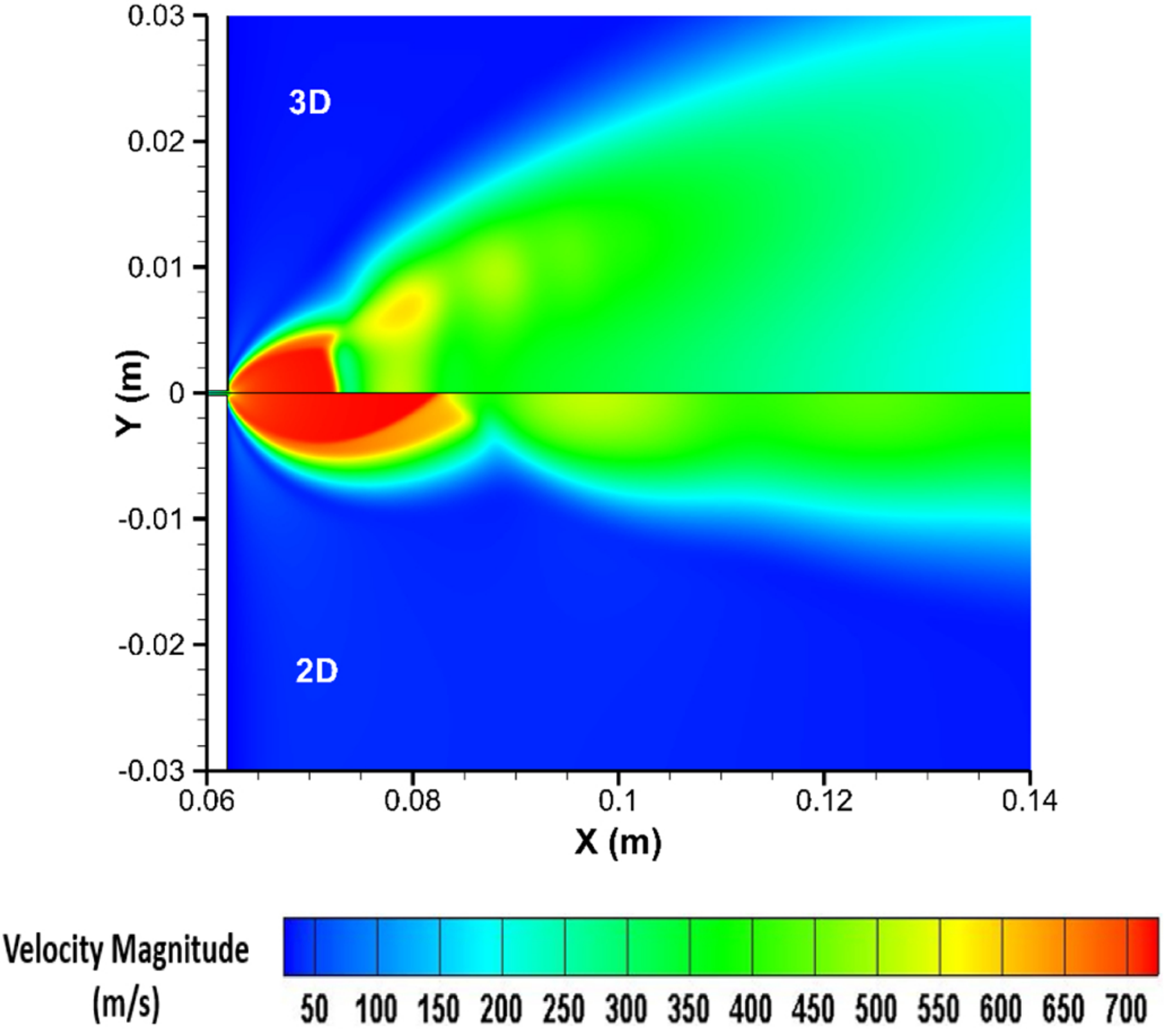
3D
2D
0.03
0.02
0.01
0
-0.01
-0.02
-0.03
Y (m)
0.06
0.08
0.1
0.12
0.14
X (m)
Velocity Magnitude
(m/s)
50 100 150 200 250 300 350 400 450 500 550 600 650 700

Figure 10

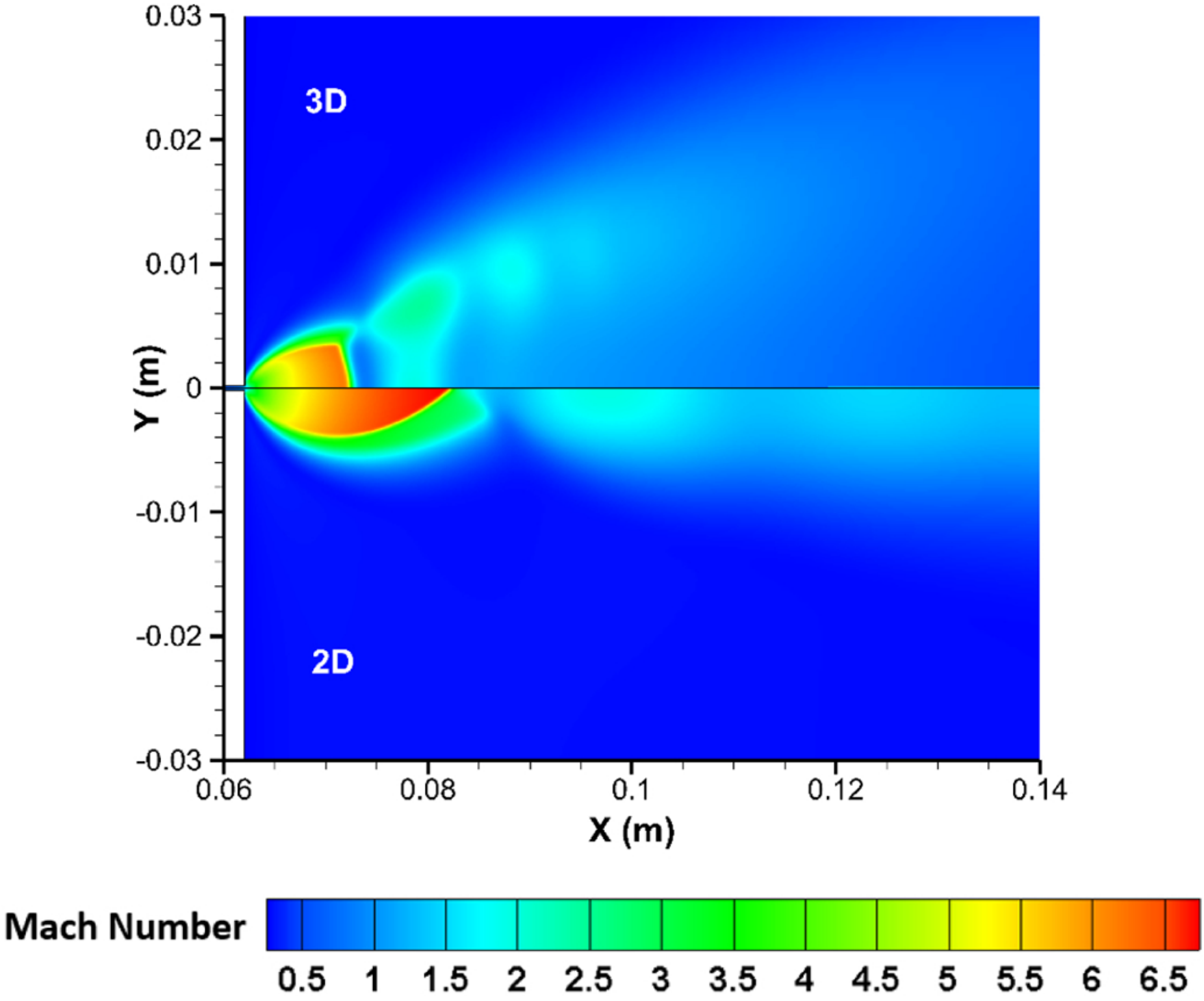
3D
2D
0.03
0.02
0.01
0
-0.01
-0.02
-0.03
Y (m)
0.06
0.08
0.1
0.12
0.14
X (m)
Mach Number
0.5
1
1.5
2
2.5
3
3.5
4
4.5
5
5.5
6
6.5

Figure 11

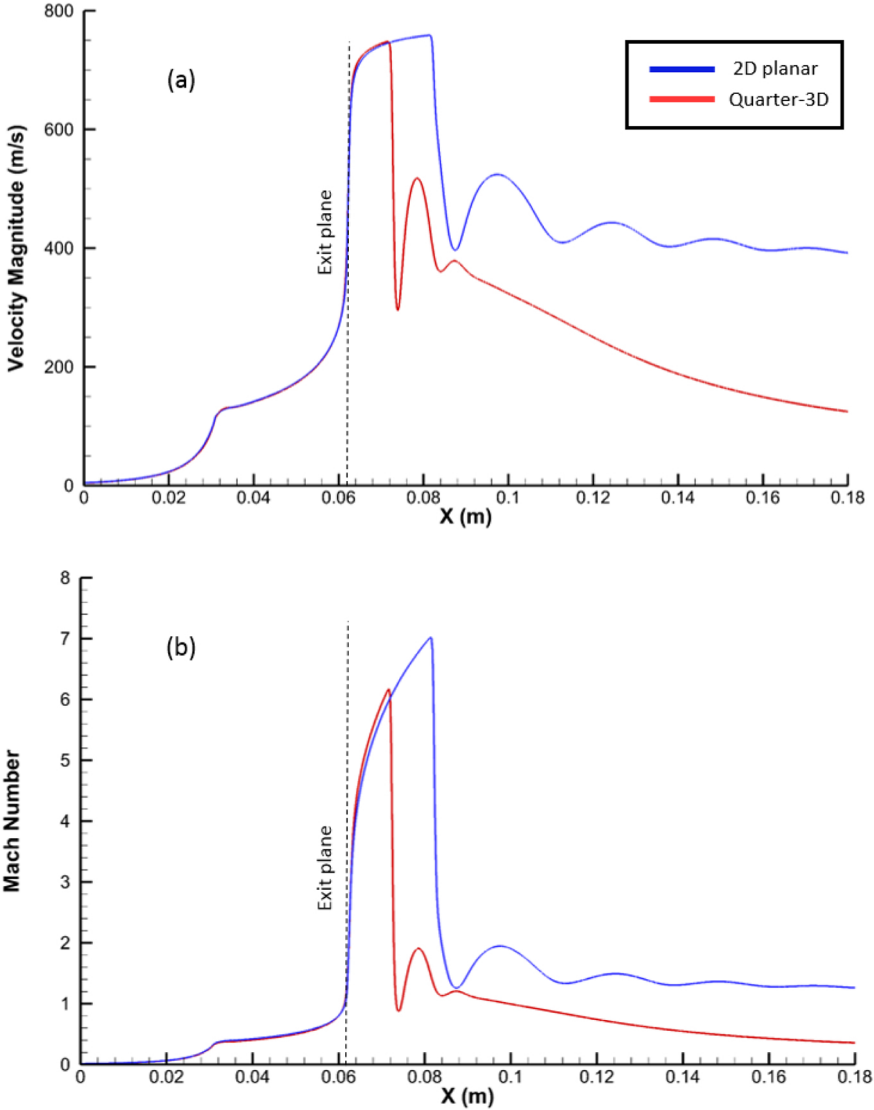
(a)
2D planar
Quarter-3D
Exit plane
Velocity Magnitude (m/s)
X (m)
(b)
Exit plane
Mach Number
X (m)

Figure 12

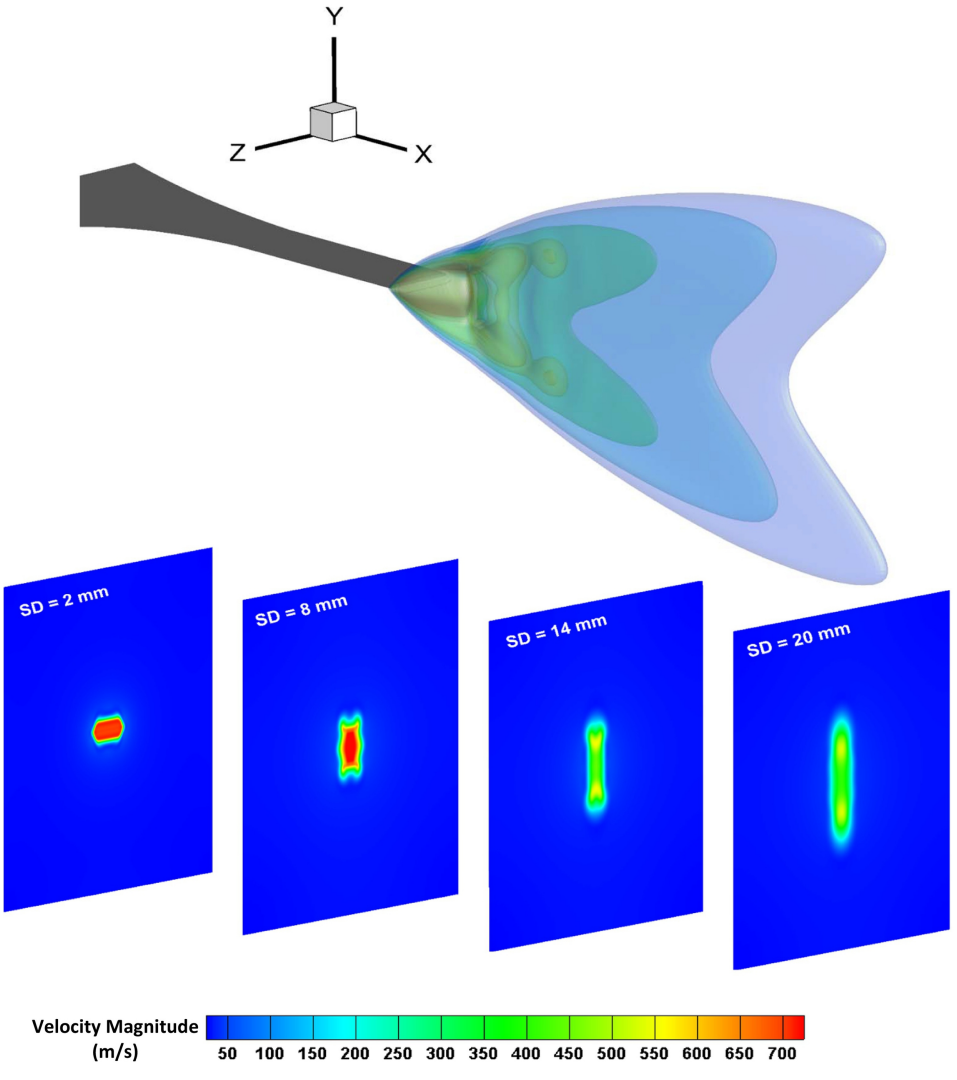
Y
Z
X
SD = 2 mm
SD = 8 mm
SD = 14 mm
SD = 20 mm
Velocity Magnitude
(m/s)
50 100 150 200 250 300 350 400 450 500 550 600 650 700

Figure 13

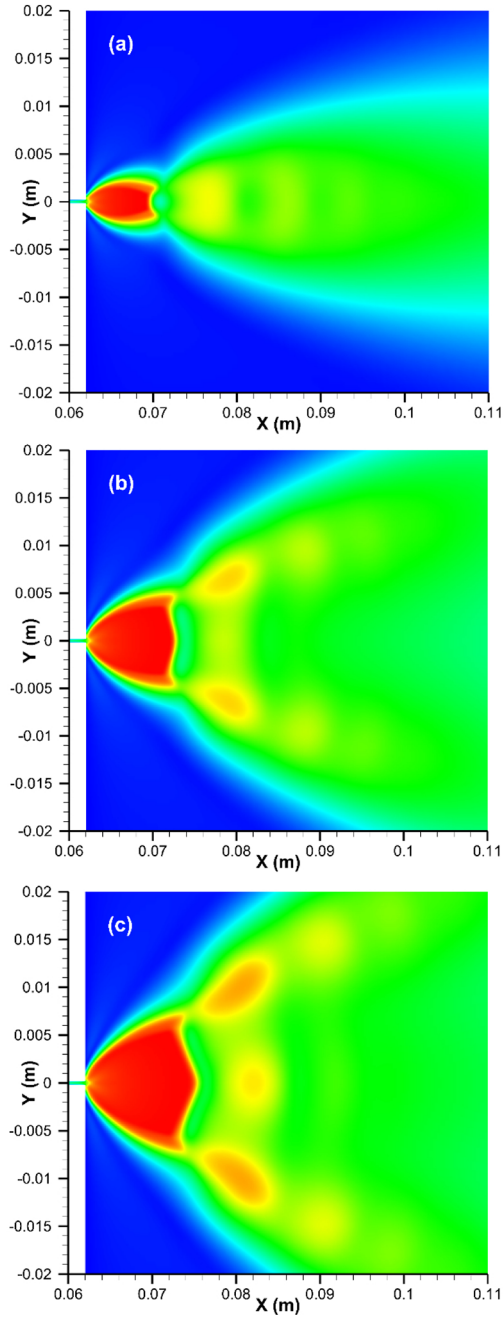
(a)
(b)
(c)
Y (m)
X (m)
0.02
0.015
0.01
0.005
0
-0.005
-0.01
-0.015
-0.02
0.06
0.07
0.08
0.09
0.1
0.11
Velocity Magnitude (m/s)
50 100 150 200 250 300 350 400 450 500 550 600 650 700

Figure 14

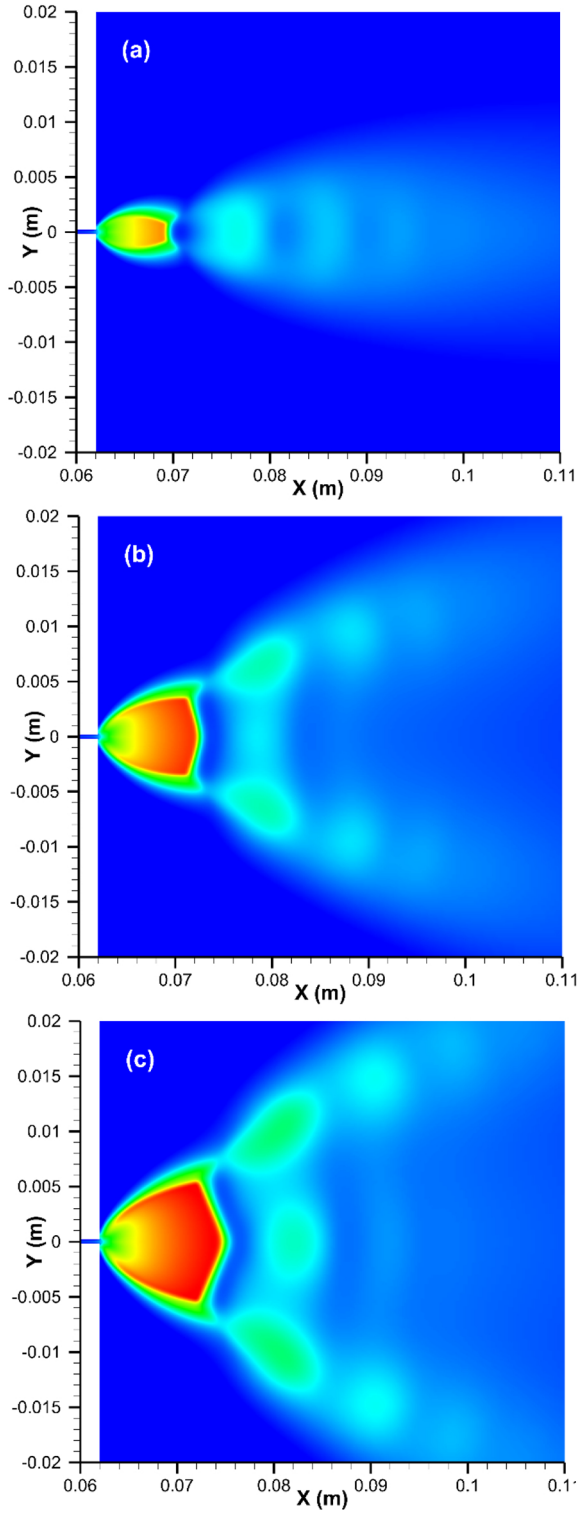
(a)
(b)
(c)
Y (m)
X (m)
0.02
0.015
0.01
0.005
0
-0.005
-0.01
-0.015
-0.02
0.06
0.07
0.08
0.09
0.1
0.11
Mach Number
0.5
1
1.5
2
2.5
3
3.5
4
4.5
5
5.5
6
6.5

Figure 15

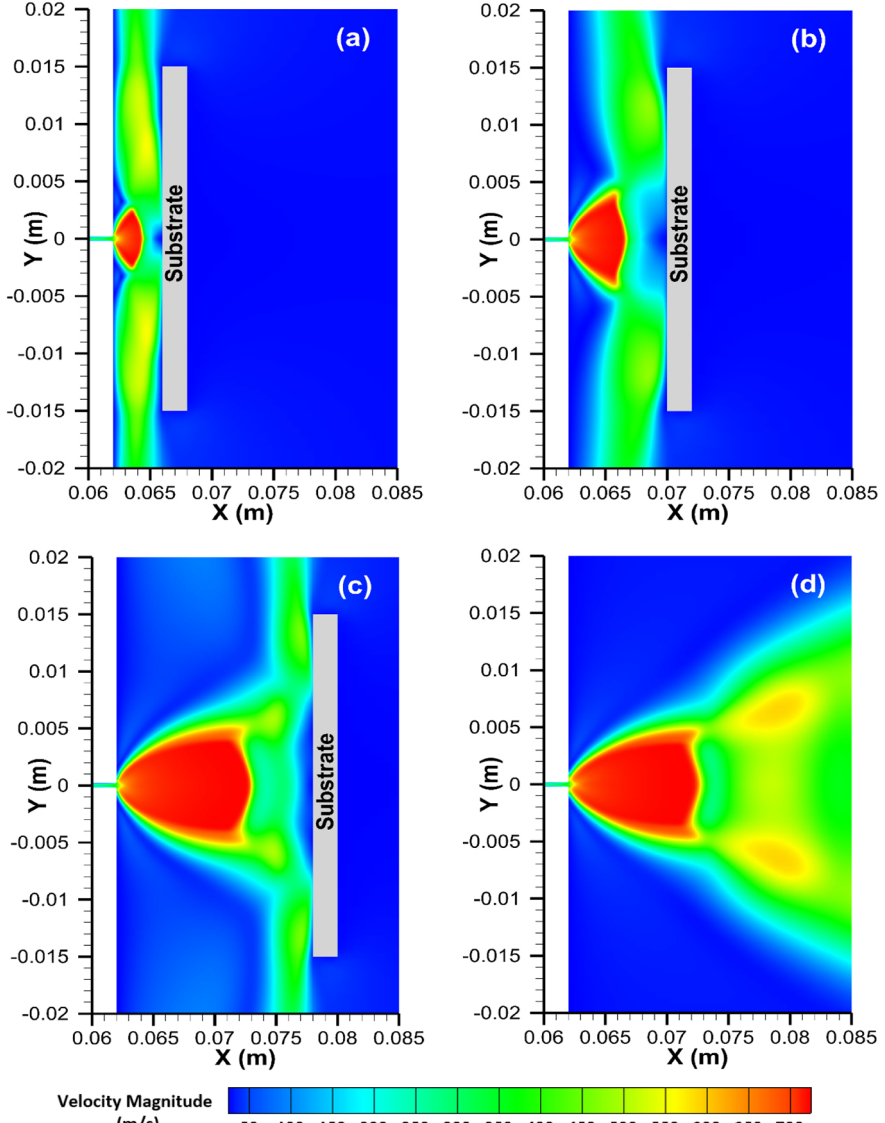
(a)
(b)
(c)
(d)
Substrate
Y (m)
X (m)
0.02
0.015
0.01
0.005
0
-0.005
-0.01
-0.015
-0.02
0.06
0.065
0.07
0.075
0.08
0.085
Velocity Magnitude
(m/s)
50
100
150
200
250
300
350
400
450
500
550
600
650
700

Figure 16

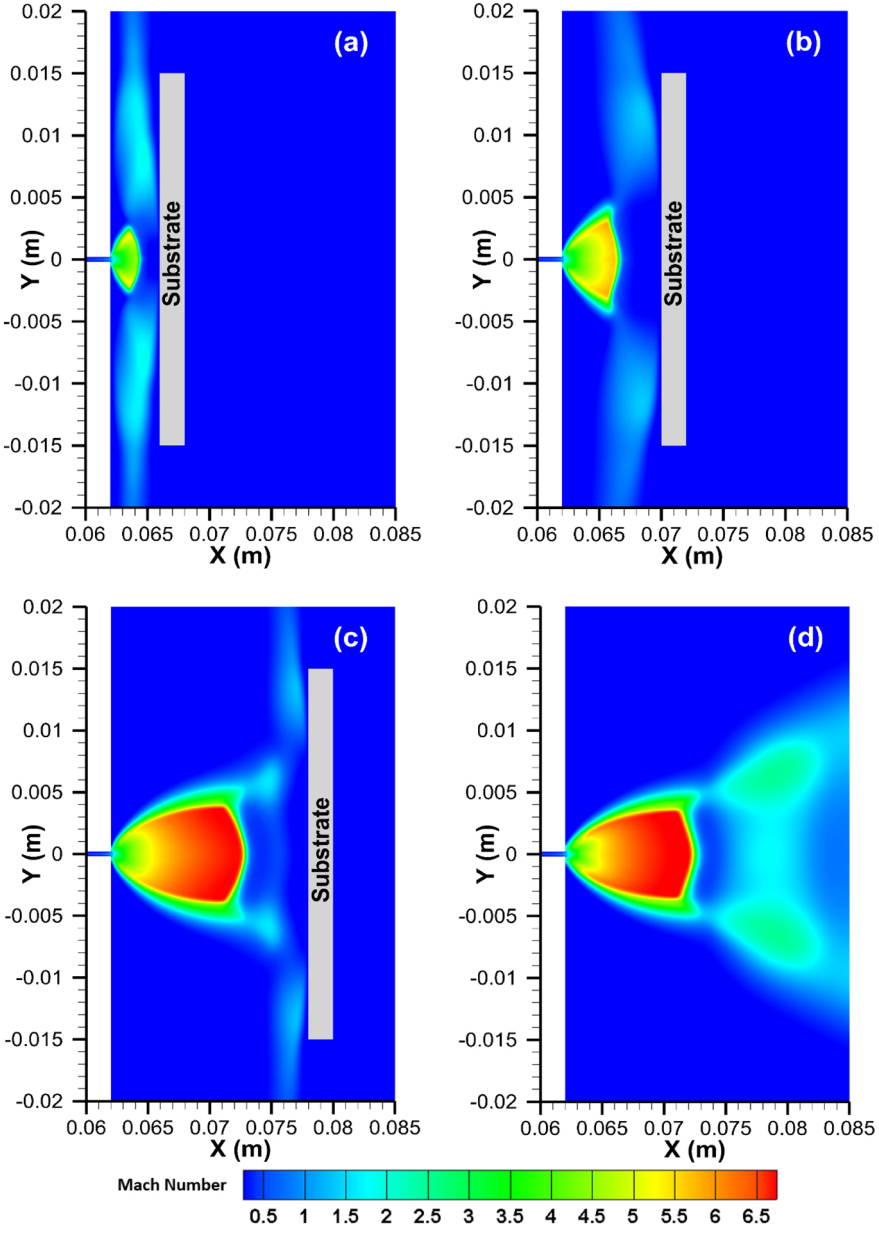
(a)
(b)
(c)
(d)
Substrate
Y (m)
X (m)
0.02
0.015
0.01
0.005
0
-0.005
-0.01
-0.015
-0.02
0.06
0.065
0.07
0.075
0.08
0.085
Mach Number
0.5
1
1.5
2
2.5
3
3.5
4
4.5
5
5.5
6
6.5

Figure 17

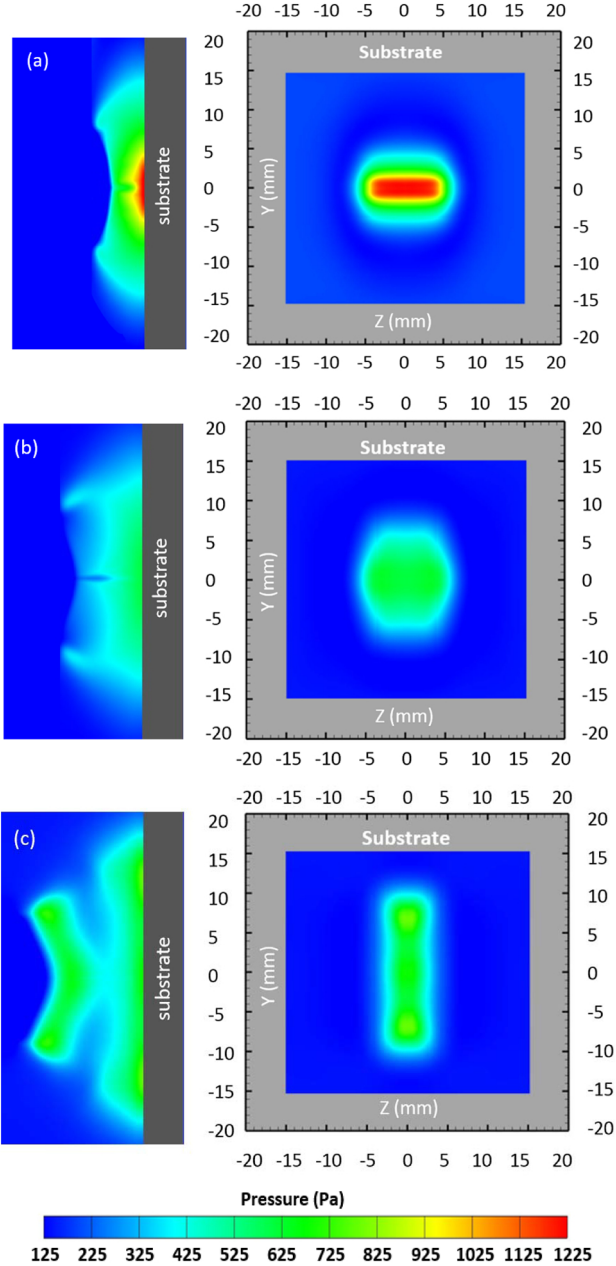
(a)
substrate
Substrate
Y (mm)
Z (mm)
(b)
substrate
Substrate
Y (mm)
Z (mm)
(c)
substrate
Substrate
Y (mm)
Z (mm)
-20 -15 -10 -5 0 5 10 15 20
Pressure (Pa)
125 225 325 425 525 625 725 825 925 1025 1125 1225

Figure 18

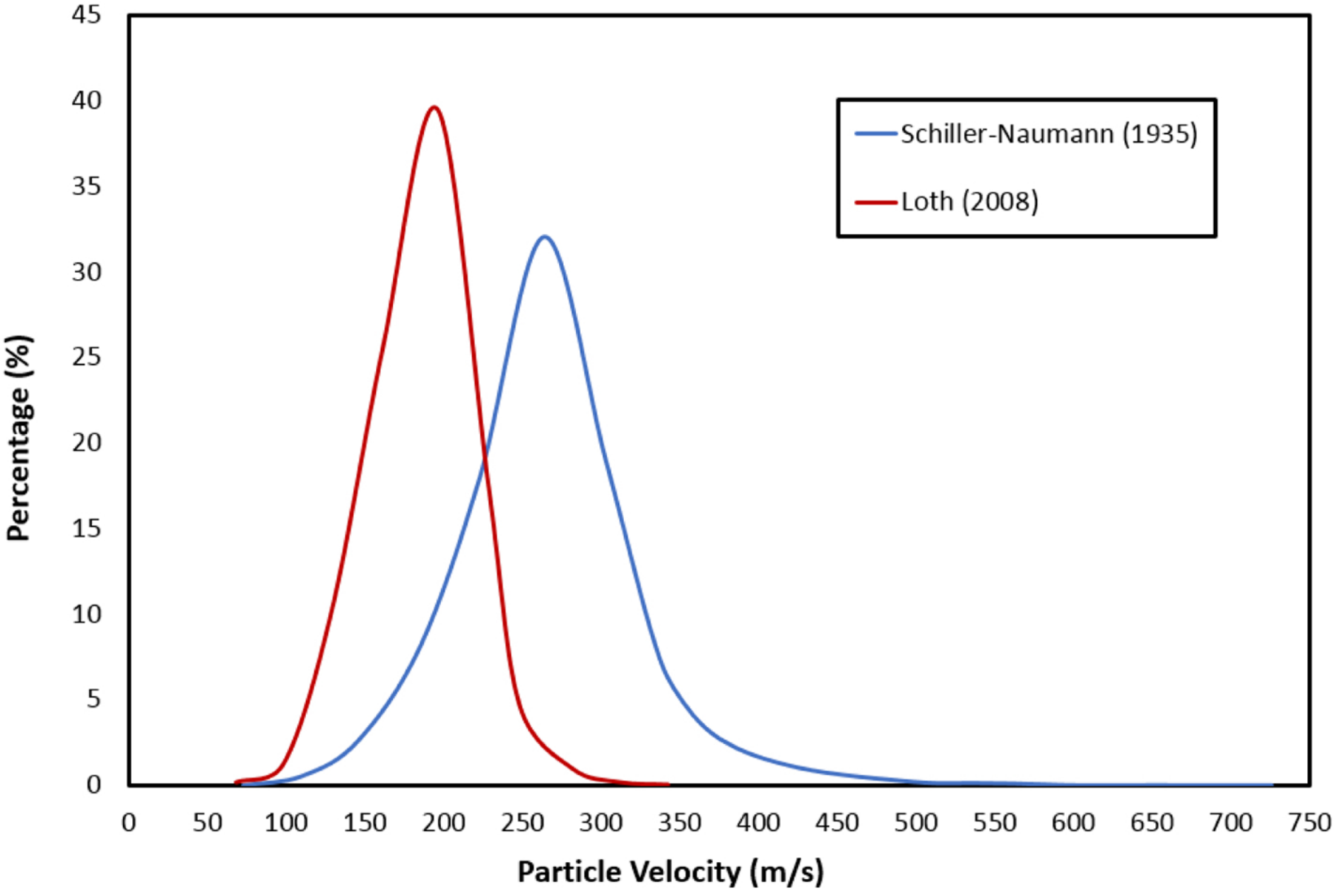
45
40
35
30
25
20
15
10
5
0
Percentage (%)
0
50
100
150
200
250
300
350
400
450
500
550
600
650
700
750
Particle Velocity (m/s)
Schiller-Naumann (1935)
Loth (2008)

Figure 19

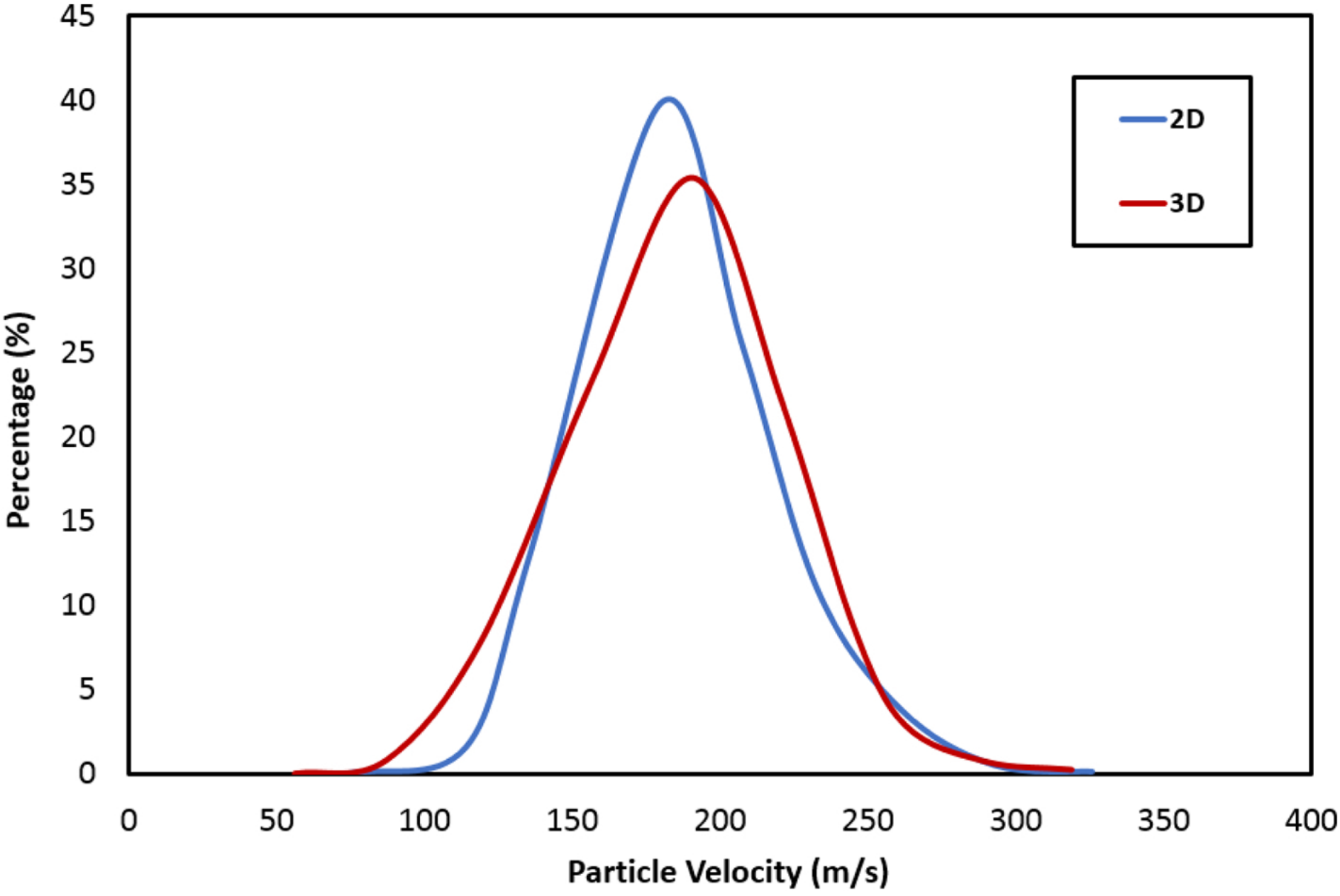
45
40
35
30
25
20
15
10
5
0
Percentage (%)
0
50
100
150
200
250
300
350
400
Particle Velocity (m/s)
2D
3D

Figure 20

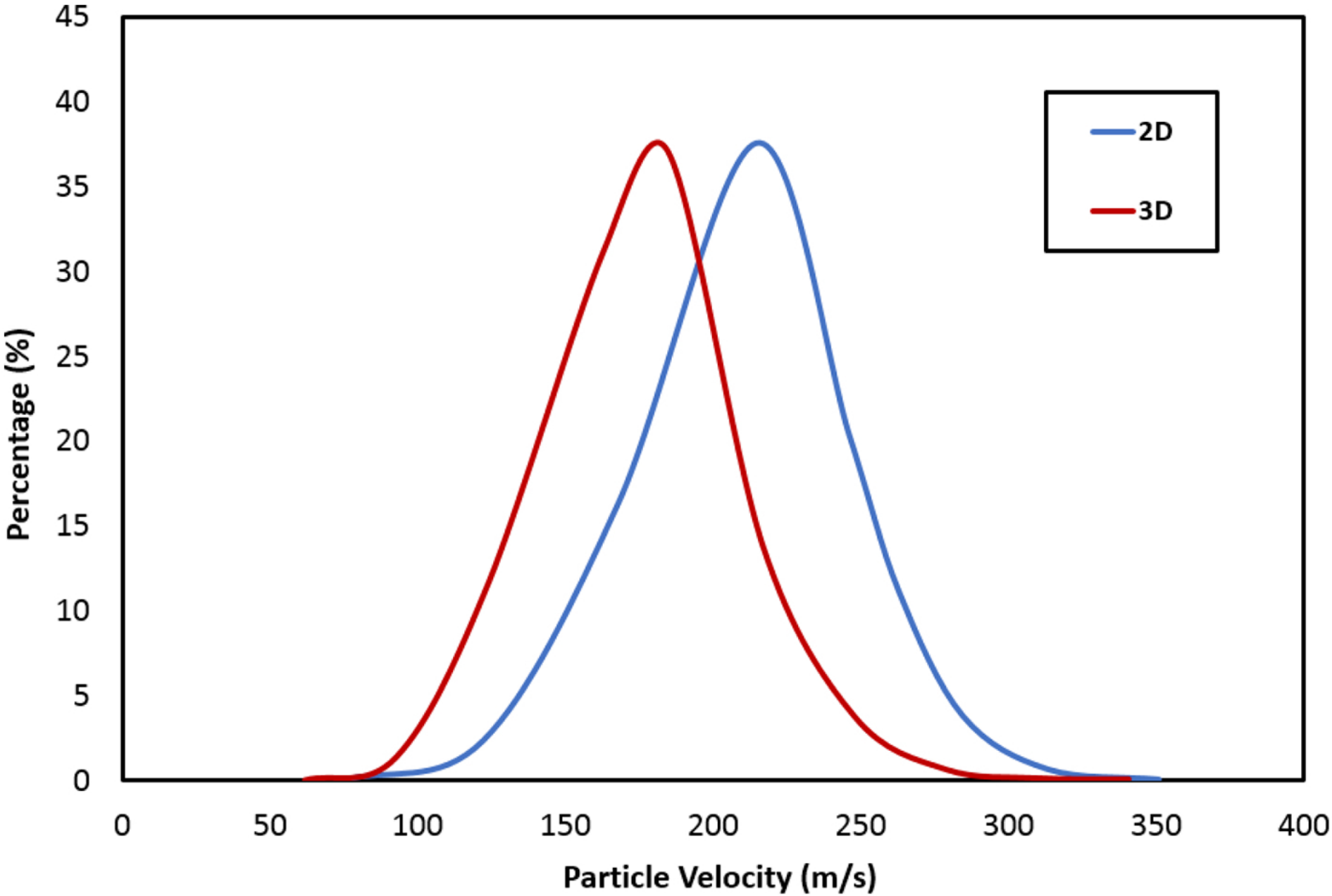
45
40
35
30
25
20
15
10
5
0
Percentage (%)
0
50
100
150
200
250
300
350
400
Particle Velocity (m/s)
2D
3D

Figure 21

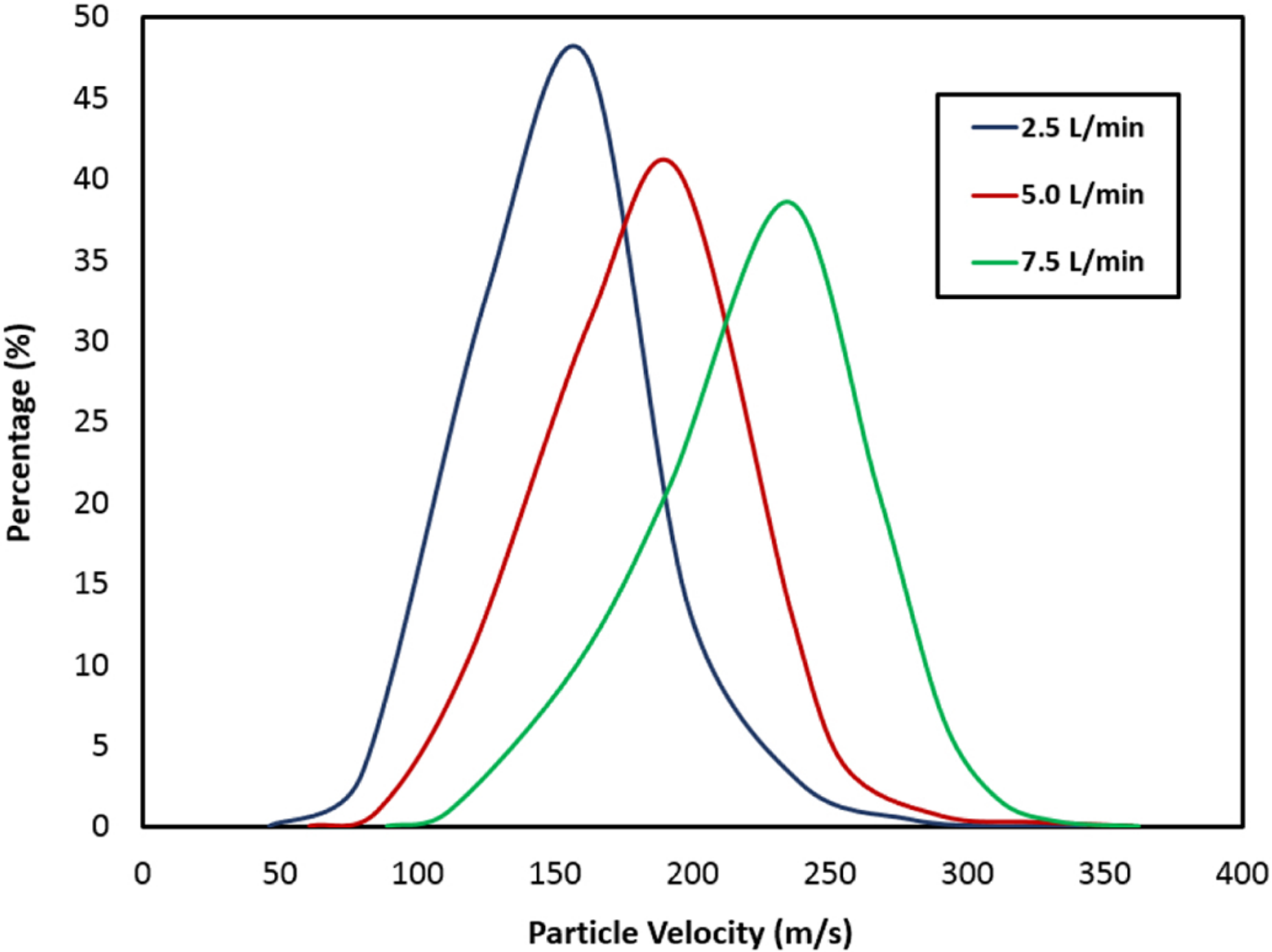
50
45
40
35
30
25
20
15
10
5
0
Percentage (%)
0
50
100
150
200
250
300
350
400
Particle Velocity (m/s)
2.5 L/min
5.0 L/min
7.5 L/min

Figure 22

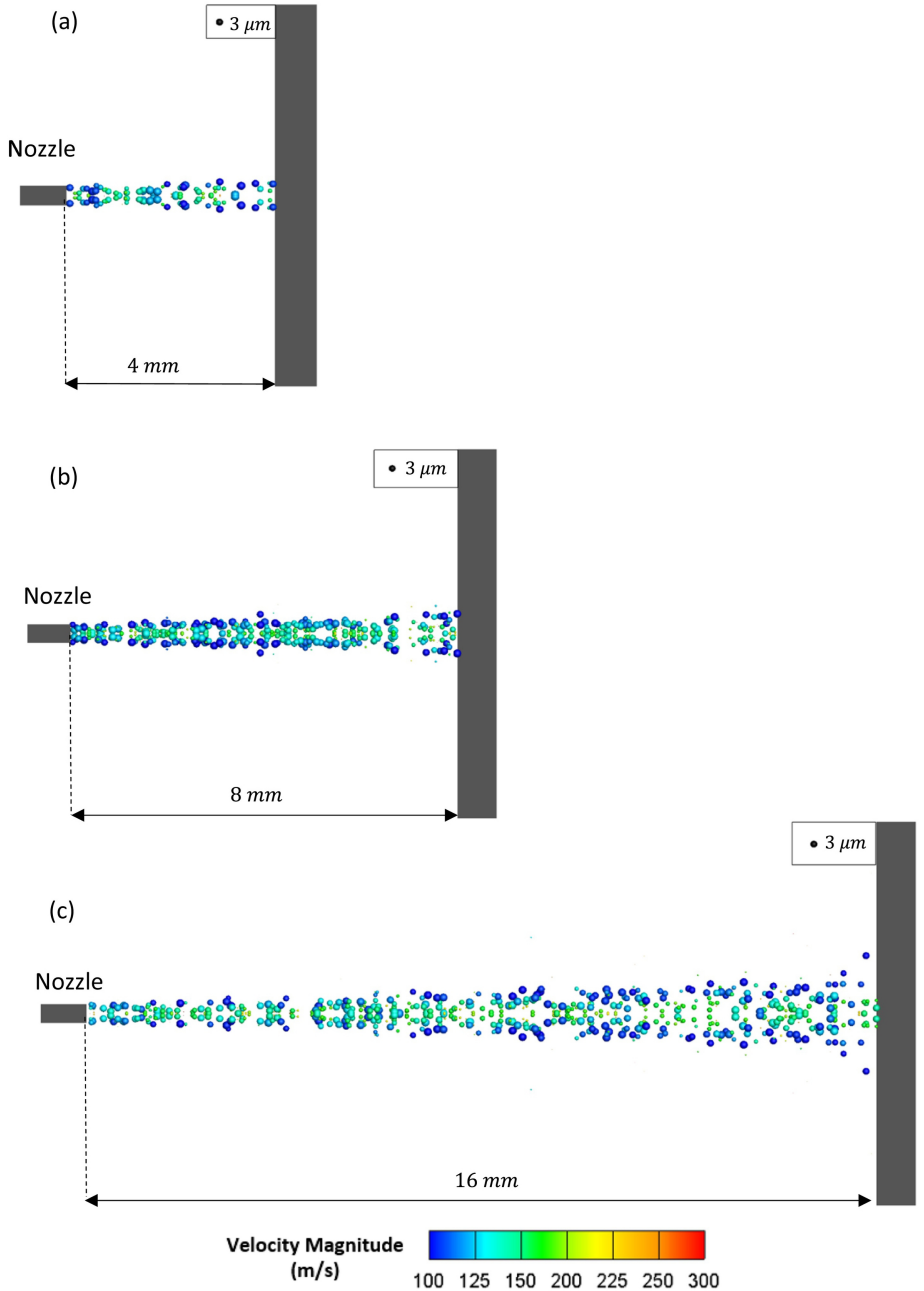
(a)
• 3 μm
Nozzle
4 mm
(b)
• 3 μm
Nozzle
8 mm
(c)
• 3 μm
Nozzle
16 mm
Velocity Magnitude
(m/s)
100 125 150 200 225 250 300

Figure 23

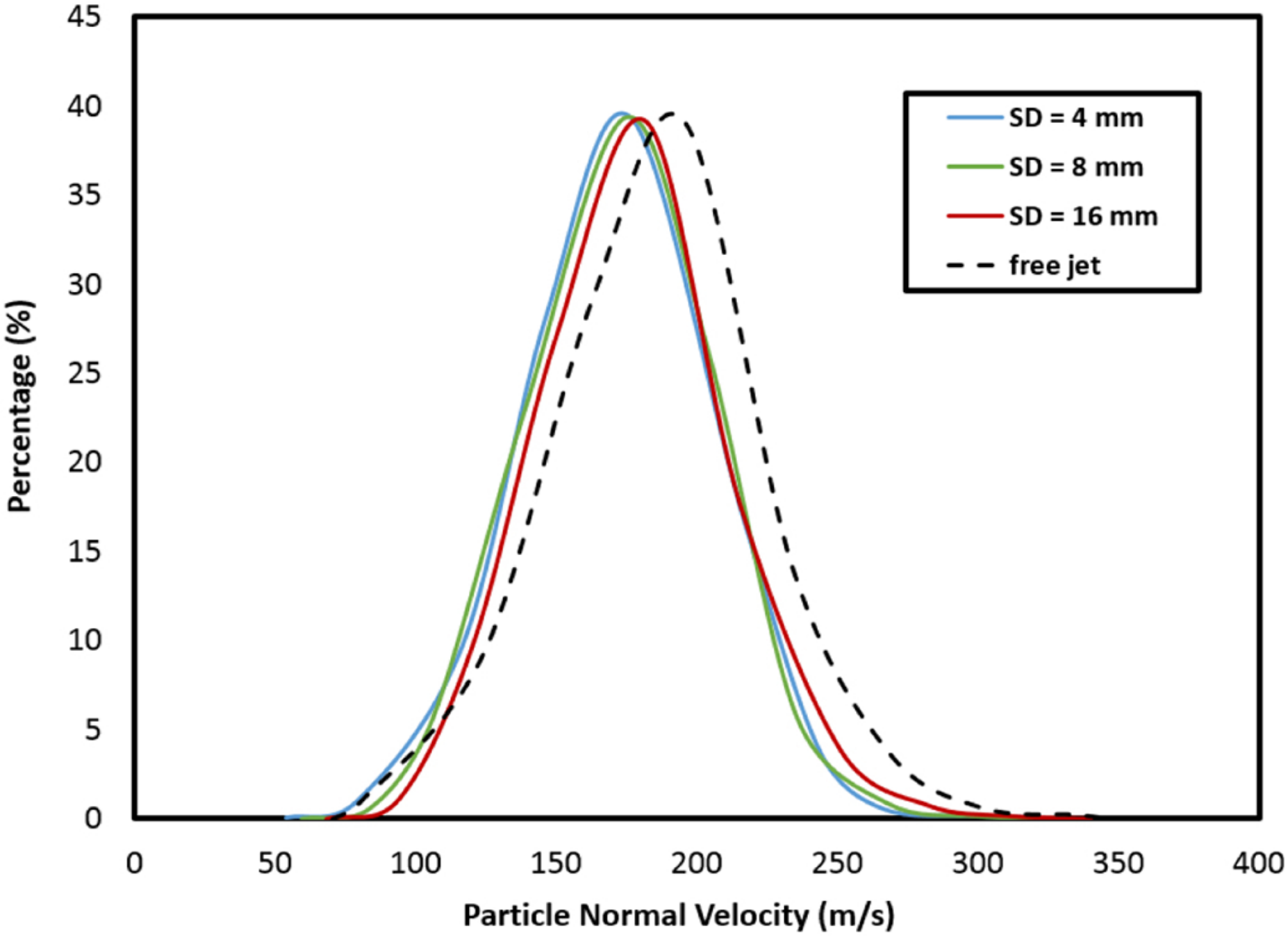
45
40
35
30
25
20
15
10
5
0
Percentage (%)
0
50
100
150
200
250
300
350
400
Particle Normal Velocity (m/s)
SD = 4 mm
SD = 8 mm
SD = 16 mm
free jet

Figure 24

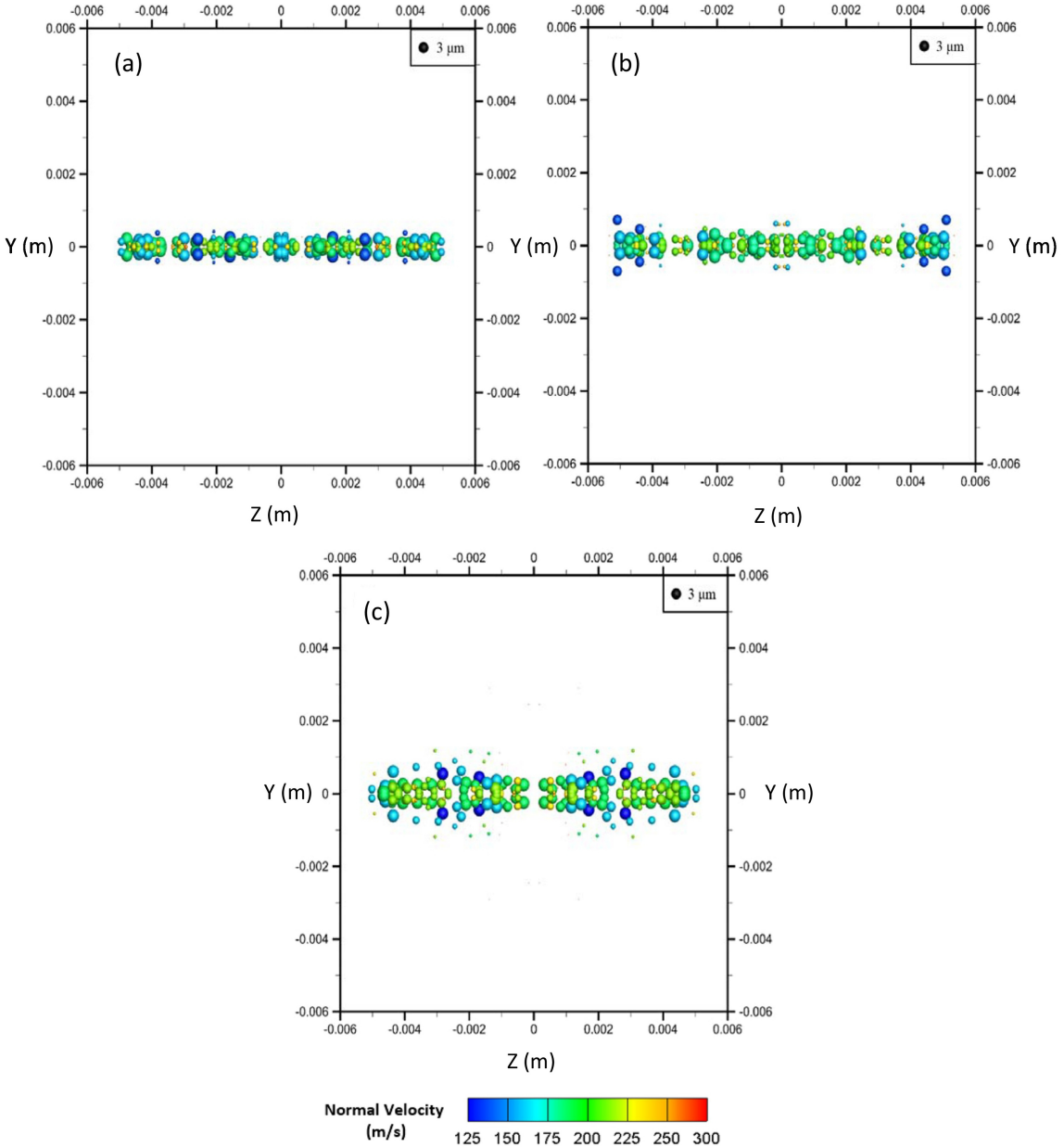
(a)
(b)
(c)
3 µm
Y (m)
Z (m)
-0.006
-0.004
-0.002
0
0.002
0.004
0.006
Normal Velocity (m/s)
125 150 175 200 225 250 300

Figure 25

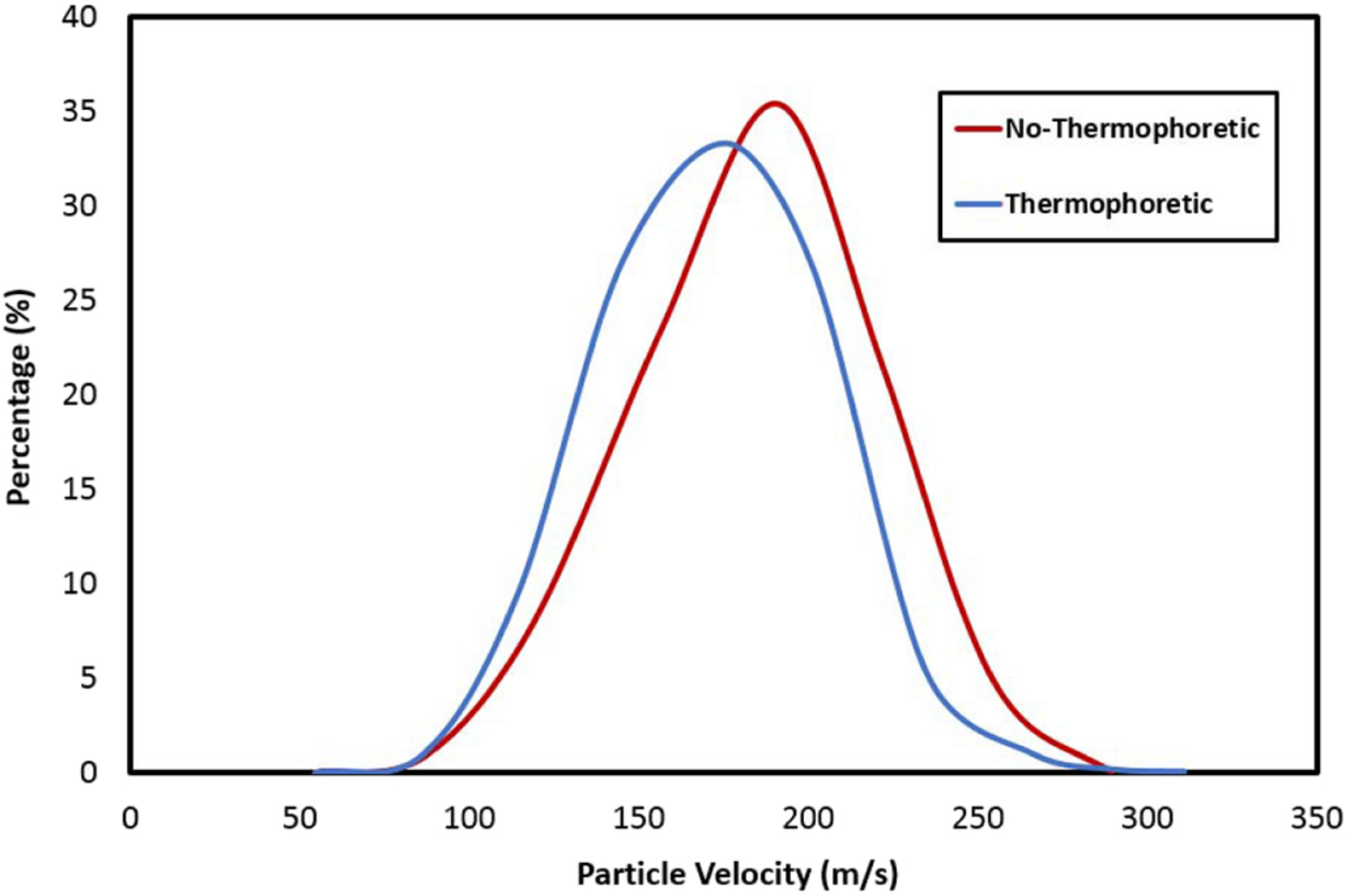
40
35
30
25
20
15
10
5
0
Percentage (%)
0
50
100
150
200
250
300
350
Particle Velocity (m/s)
No-Thermophoretic
Thermophoretic

Figure 26

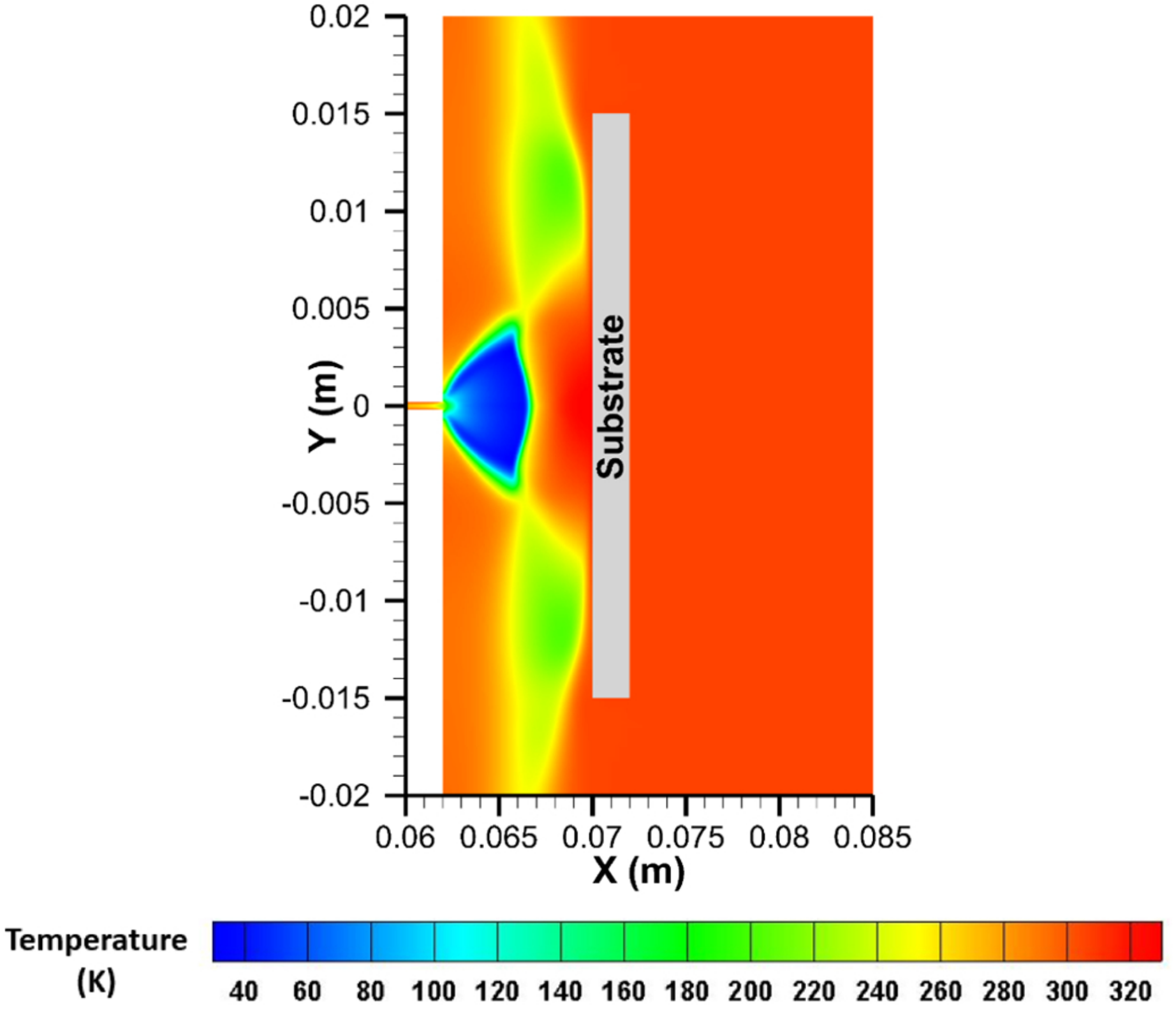
0.02
0.015
0.01
0.005
0
-0.005
-0.01
-0.015
-0.02
Y (m)
Substrate
0.06
0.065
0.07
0.075
0.08
0.085
X (m)
Temperature
(K)
40
60
80
100
120
140
160
180
200
220
240
260
280
300
320

Figure 27